

1 * Preprint uploaded to EarthArxiv. Please cite the
2 published version in G3:doi/10.1029/2020GC009364 *

3 Reconstructing Magma Storage Depths for the 2018
4 Kīlauean Eruption from Melt inclusion CO₂ Contents:
5 The Importance of Vapor Bubbles

6 P. E. Wieser¹, H. Lamadrid², J. Maclennan¹, M. Edmonds¹, S. Matthews³, K.
7 Iacovino⁴, F.E. Jenner⁵, C. Gansecki⁶, F. Trusdell⁷, R.L. Lee⁷ and E.
8 Ilyinskaya⁸

9 ¹Department of Earth Sciences, University of Cambridge, UK.

10 ²Geological Sciences, University of Missouri, 65211, US.

11 ³Johns Hopkins University, Department of Earth and Planetary Sciences, Baltimore, MD 21218, USA.

12 ⁴Jacobs, NASA Johnson Space Center, Houston, TX 77058, USA.

13 ⁵School of Environment, Earth and Ecosystem Sciences, The Open University, MK7 6AA, UK

14 ⁶Department of Geology, University of Hawai'i at Hilo, Hilo, HI 96720, USA

15 ⁷USGS Hawaiian Volcano Observatory, Hilo, HI 96720, USA

16 ⁸School of Earth and Environment, University of Leeds, UK

17 **Key Points:**

- 18 • Petrological, gaseous and geophysical observations can be reconciled by a
19 model where Fissure 8 was supplied from two summit storage reservoirs (~1–2
20 and 3–5 km depth)
- 21 • Extensive post-entrapment crystallization of melt inclusions within High-Fo
22 olivines (Fo>81.5) caused ~90% of the CO₂ to enter the vapor bubble.
- 23 • Raman analyses of vapor bubbles combined with choice of a suitable H₂O-
24 CO₂ solubility model is required to accurately determine magma storage
25 depths.

Corresponding author: P. Wieser, penny.wieser@gmail.com

Abstract

The 2018 lower East Rift Zone (LERZ) eruption and the accompanying collapse of the summit caldera marked the most destructive episode of activity at Kīlauea Volcano in the last 200 years. The eruption was extremely well-monitored, with extensive real-time lava sampling as well as continuous geodetic data capturing the caldera collapse. This multi-parameter dataset provides an exceptional opportunity to determine the reservoir geometry and magma transport paths supplying Kīlauea’s LERZ. The forsterite contents of olivine crystals, together with the degree of major element disequilibrium with carrier melts, indicates that two distinct crystal populations were erupted from Fissure 8 (termed High- and Low-Fo). Melt inclusion entrapment pressures reveal that Low-Fo olivines (close to equilibrium with their carrier melts) crystallized within the Halema’uma’u reservoir (~2 km depth), while many High-Fo olivines ($>Fo_{81.5}$; far from equilibrium with their carrier melts) crystallized within the South Caldera reservoir (~3–5 km depth). Melt inclusions in High-Fo olivines experienced extensive post-entrapment crystallization following their incorporation into cooler, more evolved melts. This favoured the growth of a CO₂-rich vapor bubble, containing up to 99% of the total melt inclusion CO₂ budget (median=93%). If this CO₂-rich bubble is not accounted for, entrapment depths are significantly underestimated. Conversely, reconstructions using equation of state methods rather than direct measurements of vapor bubbles overestimate entrapment depths. Overall, we show that direct measurements of melts and vapor bubbles by SIMS and Raman Spectroscopy, combined with a suitable H₂O-CO₂ solubility model, is a powerful tool to identify the magma storage reservoirs supplying volcanic eruptions.

Plain Language Summary

Pockets of frozen magma trapped within olivine crystals, termed “melt inclusions”, can provide information about the depths at which magma is stored beneath the surface prior to a volcanic eruption. This is because the amount of CO₂ and H₂O that can be dissolved in a melt is dependent on the pressure, and therefore the depth. We examine melt inclusions from lava flows produced during the 2018 eruption of Kīlauea Volcano. Previous work, based on geophysics, has shown that magma is stored in two main reservoirs at Kīlauea, located at ~1–2 km and ~3–

58 5 km depth. However, because many melt inclusions host almost all of their CO₂
59 within a vapor bubble, which is rarely measured, previous petrological estimates
60 of magma storage depths at Kīlauea do not align with the depths of the two reser-
61 voirs identified by geophysics. In this study, we measure the amount of CO₂ in the
62 glass and the bubble using Secondary Ion Mass Spectrometry (SIMS) and Raman
63 Spectroscopy respectively. By adding these two measurements together, we can re-
64 construct the amount of CO₂ that was present when melt inclusions were trapped.
65 Calculated depths align remarkably well with geophysical estimates, and demon-
66 strate that the 2018 eruption was supplied by both magma storage reservoirs.

67 1 Introduction

68 The 2018 lower East Rift Zone (LERZ) eruption was the largest and most
69 destructive in the last 200 years of activity at Kīlauea Volcano, Hawai'i (Neal et
70 al., 2019), accompanied by the highest co-eruptive fluxes of SO₂ ever measured at
71 Kīlauea (up to 200 kt a day; Kern et al., 2020; Whitty et al., 2020), and very high
72 lava effusion rates (100-300 m³/s; Neal et al., 2019; Patrick et al., 2019). Before the
73 onset of this new eruptive episode in May 2018, Kīlauea had been erupting near-
74 continuously for 35 years on the middle East Rift Zone (ERZ) at Pu'u Ō'ō cone and
75 surrounding vents, located approximately ~20 km east of Kīlauea's summit (1983–
76 2018), and ~24 km uprift of the 2018 eruption site (Fig. 1b). From 2008 to 2018,
77 a persistently active lava lake was also present within Halema'uma'u (HMM) pit
78 crater, located in the south west area of Kīlauea's summit caldera (Fig. 1b).

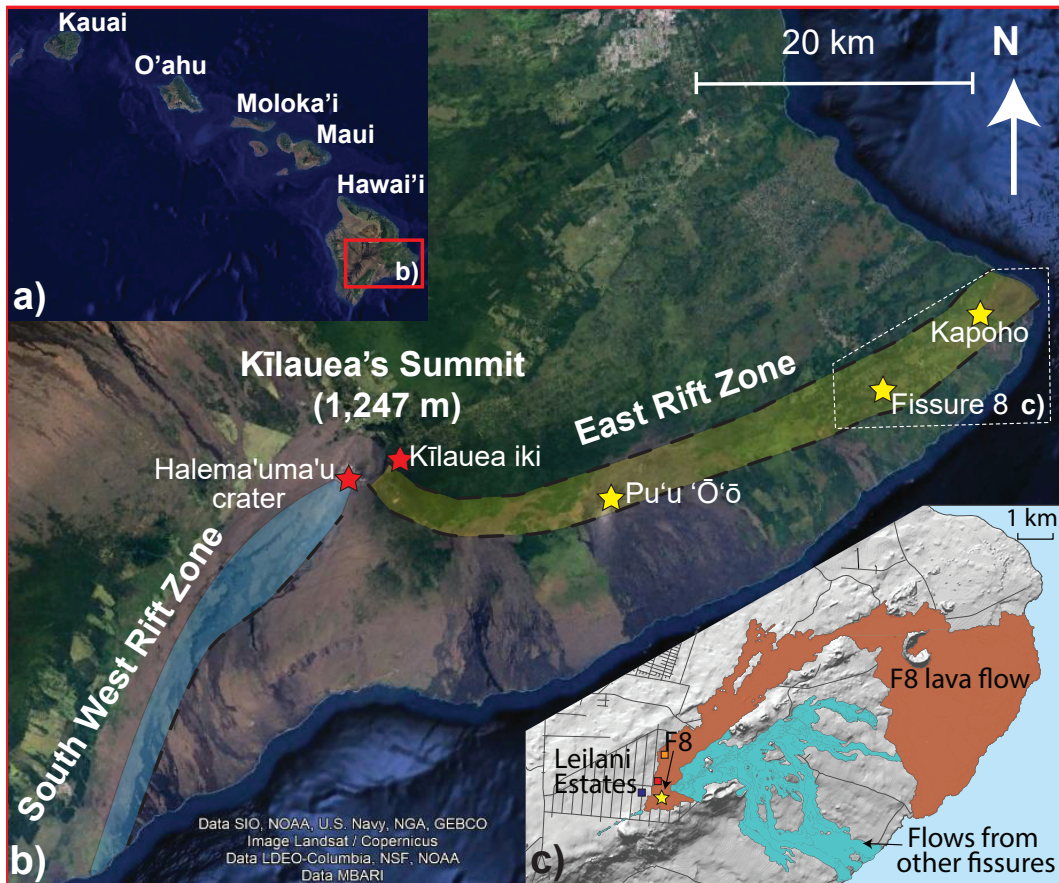


Figure 1. Map of Kīlauea Volcano (b), located on the southwest of the island of Hawai'i (a). Two prominent rift zones radiate from Kīlauea's summit caldera (b). The 2018 eruption occurred within the Leilani Estates subdivision on the lower East Rift Zone (LERZ; expanded region in c). The lava flows from Fissure 8 (marked with a yellow star) are colored deep orange, while flows from Fissures 1–7, and 9–24 are colored light blue. Sample locations are marked with squares (blue=May, 2018, red=July, 2018, orange=Aug, 2018). Base maps for a) and b) are from Google Earth, and the map in c) is adapted from Patrick et al. (2019).

79 The 2018 eruption was preceded by swarms of lower-crustal earthquakes at
 80 ~6–12 km depth beneath Kīlauea's summit area on March 7th, April 11th, and
 81 April 18th, 2018 (Flinders et al., 2020). This inflation has been variably interpreted
 82 to result from a short-term increase in magma supply (Flinders et al., 2020), or a
 83 decrease in the output of magma along the ERZ to Pu'u 'Ō'ō, leading to magma
 84 backing up within the summit reservoir (Patrick et al., 2020). On March 13th,
 85 2018, inflation was recorded by tiltmeters located at Kīlauea's summit. Inflationary

86 ground deformation also began at Pu'u 'Ō'ō, suggesting that excess magma was
87 accumulating beneath this vent (Neal et al., 2019). The pressurization at these two
88 locations continued throughout March and April, demonstrated by the rise of the
89 lava pond at Pu'u 'Ō'ō, and overflows of the summit lava lake in mid-late April. On
90 April 30th, the crater floor at Pu'u 'Ō'ō collapsed, followed by an eastward migra-
91 tion of seismicity along the rift zone, consistent with the propagation of a dyke (Neal
92 et al., 2019). A hazard notice released early in the morning of May 1st warned the
93 residents of Lower Puna to be alert, as a large area along the ERZ east of Pu'u 'Ō'ō
94 was at risk from a new outbreak of lava. Following the appearance of ground cracks
95 in the Leilani Estates subdivision (Fig. 1c) on May 2nd, lava reached the surface
96 just before 5 pm on May 3rd (Neal et al., 2019). Over the next few days, multiple
97 fissures opened, preceded by gas emissions and ground cracking. In all, 24 fissures
98 opened between the 3rd and 27th of May 2018.

99 Activity between the 3rd and 9th of May, classified as Early Phase 1 by
100 Gansecki et al. (2019), was characterized by the eruption of spatter mounds and
101 sluggish, slow-moving lava flows. This relatively evolved magma (mean $\text{SiO}_2=51$
102 wt% and $\text{MgO}=4$ wt%; Lee et al., 2019; Gansecki et al., 2019) is thought to have
103 formed by differentiation within LERZ storage reservoirs over decades to centuries
104 (Neal et al., 2019). Throughout May, the compositions of erupted melts and crys-
105 tals became increasingly primitive as summit-derived magma flushed out the LERZ
106 storage reservoirs, with the exception of the involvement of an andesitic composition
107 erupted in mid to late May (Gansecki et al., 2019). The eruption of hotter, less vis-
108 cous lava led to the generation of fast-moving lava flows on May 18th, which reached
109 the coast five days later (Neal et al., 2019, Fig. 1c). By May 28th, activity had lo-
110 calized at Fissure 8 (F8), with the effusion of fast-flowing magma in a channelized
111 flow (Patrick et al., 2019). Activity ended abruptly on August 4th, by which time
112 F8 had erupted $\sim 1.5 \text{ km}^3$ of lava (Kauahikaua & Trusdell, 2020).

113 Despite the abundant geophysical and geochemical observations made during
114 the LERZ eruption, the source of the magma erupted at F8 from late May-August
115 2018 has not yet been established. It is generally accepted that two main reservoirs
116 are located beneath Kilauea's summit. The shallower Halema'uma'u (HMM) reser-
117 voir is recognised as an inflation source located beneath the eastern rim of the HMM
118 crater, and is thought to be centred at $\sim 0.5\text{--}2$ km depth (Anderson et al., 2019;

119 Cervelli & Miklius, 2003; Baker & Amelung, 2012; Fiske & Kinoshita, 1969), while
120 the deeper South Caldera (SC) reservoir manifests as an inflation source located
121 beneath the southern portion of the caldera, at $\sim 3\text{--}5$ km depth (Baker & Amelung,
122 2012; Poland et al., 2015). The 2018 LERZ eruption was accompanied by large-scale
123 subsidence of the caldera floor centred around the HMM crater (500 m in certain
124 locations; Neal et al., 2019), which has been attributed to magma withdrawal from
125 the underlying HMM reservoir to feed the effusion of lava from F8 (Anderson et al.,
126 2019). However, recent estimates of the total SO_2 emissions requires the erupted vol-
127 ume to be approximately twice the modelled volume loss from the HMM reservoir,
128 suggesting that a second magma source was involved (Kern et al., 2020).

129 Additionally, the erupted crystal cargo from F8 contained some of the most
130 forsteritic olivines ($\text{Fo}_{88\text{--}89}$) erupted at Kīlauea since 1974, which must have grown
131 in melts with 13–14 wt% MgO (Gansecki et al., 2019). Some of these crystals also
132 contain prominent kink bands (Gansecki et al., 2019), indicating that their crystal
133 lattices have been deformed (Wieser, Edmonds, et al., 2020). Previous work has
134 suggested that highly forsteritic, deformed olivines are derived from the deeper,
135 SC reservoir at 3–5 km depth (Helz et al., 2014, 2015; Wieser et al., 2019; Wieser,
136 Edmonds, et al., 2020), or Kīlauea’s deep rift zones at 6–9 km depth (Clague & Den-
137 linger, 1994; Vinet & Higgins, 2010). Alternatively, Lynn et al. (2017) suggest that
138 highly forsteritic olivines from the Keanakāko’i Tephra may originate from deeper
139 crustal storage reservoirs, perhaps located near the base of the volcanic pile at $\sim 8\text{--}10$
140 km depth.

141 Our study utilizes the strong pressure dependence of the solubility of CO_2 (and
142 H_2O) in silicate melts to determine the pressures at which pockets of melt, termed
143 melt inclusions, were trapped within olivine crystals. Through prior constraints
144 on the density profile of the crust, entrapment pressures from F8 melt inclusions
145 erupted in late May, mid-July and early August 2018 can be converted into entrap-
146 ment depths. In turn, these depths can be compared to geophysical estimates of the
147 depths of the main magma storage regions at Kīlauea to determine the source(s) of
148 magma erupted at F8.

2 Melt Inclusion Entrapment Pressures

2.1 The Importance of Vapor Bubbles

The solubility of pure CO₂ and H₂O in silicate melts is dependent on the pressure, the major element content of the melt, and the melt temperature. Assuming that a melt was saturated in a CO₂-H₂O fluid phase at the time of melt inclusion formation, the pressure at which a melt inclusion was trapped can be calculated by reconstructing its initial volatile and major element composition. In relatively water-poor systems like Kilauea, where melts contain <1 wt% H₂O (Dixon et al., 1991; Clague et al., 1995; Sides, Edmonds, Maclennan, Swanson, & Houghton, 2014; Sides, Edmonds, Maclennan, Houghton, et al., 2014; Tucker et al., 2019; Wallace & Anderson, 1998), the entrapment pressure is most sensitive to the CO₂ content of the melt, and its major element composition. Variations in melt H₂O content between 0–1 wt% have a relatively small effect on the entrapment pressure (except at very low CO₂ contents; see Supporting Information Fig. S1; Newman & Lowenstern, 2002).

However, estimating the CO₂ content of a melt inclusion at the point of entrapment is not straightforward. The host crystal may experience a period of cooling after the melt inclusion was trapped, leading to the growth of olivine on the walls of the inclusion (termed post-entrapment crystallization, or PEC; Roedder, 1984; Danyushevsky et al., 2000; Anderson & Brown, 1993). The precipitation of denser olivine from the silicate melt, combined with the differential thermal contraction of the melt phase and the host olivine, causes the internal pressure of the melt inclusion to drop, driving the growth of a vapor bubble (Roedder, 1979; Anderson, 1974; Anderson & Brown, 1993). Combined with a reduction in the solubility of CO₂ associated with major element changes during PEC, these processes cause CO₂ to migrate from the melt phase into the bubble (Steele-Macinnis et al., 2011; Sides, Edmonds, Maclennan, Houghton, et al., 2014; Maclennan, 2017; Aster et al., 2016). An additional phase of bubble growth is caused by the differential thermal contraction of the melt inclusion and the host olivine during syn-eruptive cooling from high magmatic temperatures (~1150° C at F8; Helz & Thornber, 1987; Gansecki et al., 2019) to the glass transition temperature (~725°C; Ryan & Sammis, 1981).

180 Unfortunately, the vast majority of published volatile contents in melt in-
181 clusions globally, and at Kilauea, only measured CO₂ in the glass phase, using
182 techniques such as secondary-ion mass spectrometry (SIMS), or Fourier transform
183 infrared spectroscopy (FTIR; Bennett et al., 2019; Ruth et al., 2018; Sides, Ed-
184 monds, Maclennan, Houghton, et al., 2014; Sides, Edmonds, Maclennan, Swanson,
185 & Houghton, 2014). Given that recent work has shown that ~40–90% of the total
186 CO₂ budget of melt inclusions may be held within the vapor bubble (Hartley et al.,
187 2014; Wallace et al., 2015; Moore et al., 2015; Rasmussen et al., 2020), entrapment
188 pressures from studies neglecting vapor bubble carbon must be viewed as minimum
189 estimates (Anderson & Brown, 1993; Ruth et al., 2018).

190 **2.2 Reconstructing Vapor Bubble CO₂**

191 Several approaches have been used to explore the contribution of vapor bubbles
192 to the CO₂ budget of Hawaiian melt inclusions. Anderson and Brown (1993) theo-
193 retically reconstruct vapor bubble CO₂ by assuming that the melt and vapor bubble
194 were in chemical equilibrium at high magmatic temperatures prior to syn-eruptive
195 quenching. Specifically, they calculated melt inclusion internal pressures from glass
196 CO₂ contents, and used these pressures to determine the molar volume of CO₂ in
197 vapor bubbles using the CO₂ equation of state (EOS). They converted their molar
198 volumes into CO₂ concentrations assuming that bubbles occupied 0.5 vol% of the
199 melt inclusion prior to quenching, and added these values to measurements of glass
200 CO₂ concentrations. Riker (2005) used a similar method to reconstruct bubble car-
201 bon for melt inclusions from the 1859 eruption of Mauna Loa. However, instead of
202 using a fixed bubble volume, they account for the differential amounts of cooling
203 and PEC experienced by erupted crystals, and calculate the bubble volumes prior to
204 quench-induced expansion as a function of the drop in temperature (ΔT) between
205 the melt inclusion at the point of entrapment and eruption ($\text{VB vol\%} = 0.0162 \Delta T$
206 $- 0.0016$). More recently, Tucker et al. (2019) theoretically reconstructed bubble
207 carbon contents for a large suite of melt inclusions from several Hawaiian volcanoes,
208 including 167 from Kilauea. However, instead of estimating the size of the vapor
209 bubble prior to syn-eruptive quenching as in Anderson and Brown (1993) and Riker
210 (2005), they used observed bubble volumes to convert CO₂ densities obtained from
211 the EOS into bubble CO₂ concentrations. This approach is problematic because ex-

212 pansion of the bubble during syn-eruptive cooling and quenching continues until the
213 glass transition temperature, while CO₂ diffusion through the melt into the bubble
214 may effectively cease at a higher temperature. Thus, the final stages of bubble ex-
215 pansion will occur without concurrent CO₂ diffusion from the glass into the bubble,
216 meaning that the EOS method will overpredict the amount of CO₂ in the bubble
217 (Anderson & Brown, 1993; Maclennan, 2017; Rasmussen et al., 2020).

218 The total amount of CO₂ within melt inclusions can also be determined using
219 experimental homogenization techniques, where crystals containing melt inclusions
220 are heated to magmatic temperatures. This drives the dissolution of the olivine
221 rim precipitated during PEC, which changes the chemistry and volume of the melt
222 inclusion so that CO₂ held within the vapor bubble dissolves back into the melt.
223 Following rapid quenching, the glass phase of these rehomogenized melt inclusions
224 can be analyzed by SIMS or FTIR (Esposito et al., 2012; Rasmussen et al., 2020;
225 Skirius et al., 1990; Tuohy et al., 2016; Wallace et al., 2015). However, experimental
226 homogenization can lead to H₂O loss, excess dissolution of olivine on the walls of
227 the melt inclusion, and loss of mineral and melt inclusion zoning, which degrades
228 the overall utility of the melt inclusion record (Rasmussen et al., 2020; Tuohy et al.,
229 2016). Additionally, it is not always possible to fully dissolve the original bubbles,
230 and new bubbles containing CO₂ may nucleate upon quench (Wallace et al., 2015;
231 Tuohy et al., 2016; Skirius et al., 1990; Rasmussen et al., 2020).

232 Most recently, the density of CO₂ in vapor bubbles has been measured di-
233 rectly using Raman Spectroscopy (Esposito et al., 2011; Steele-Macinnis et al.,
234 2011; Hartley et al., 2014; Moore et al., 2015, 2018; Aster et al., 2016; Taracsák et
235 al., 2019). The Raman spectrum of CO₂ consists of two peaks nominally at 1285
236 cm⁻¹ and 1388 cm⁻¹ at 1 bar (see Supporting Information Fig. S2), resulting from
237 the interaction of a symmetrical stretching mode and an active bending mode in
238 the CO₂ molecule by a process known as Fermi resonance (Rosso & Bodnar, 1995;
239 Lamadrid et al., 2017; Fermi, 1931). Hence, collectively, these peaks are referred to
240 as the Fermi diad (FD), and the distance between the peak centres is the Fermi diad
241 splitting (Δ). However, while it is well accepted that Δ correlates with CO₂ den-
242 sity (ρ_{CO_2}), there are a number of different parameterizations for this relationship
243 in the literature (Wang et al., 2019; Rosso & Bodnar, 1995; Lamadrid et al., 2017;
244 Kawakami et al., 2003, and refs. within). The diversity of published densimeters

245 reflects different instrument hardware, as well as the choice of analytical conditions
 246 (Lamadrid et al., 2017). Thus, the approach used by a number of studies where a
 247 densimeter is chosen from the literature to convert measurements of Δ to ρ_{CO_2} on a
 248 different Raman instrument from the one used to calibrate the densimeter results in
 249 large systematic uncertainties in the absolute density of CO_2 (e.g., Venugopal et al.,
 250 2020; Taracsák et al., 2019; Hartley et al., 2014). For example, $\Delta=102.8 \text{ cm}^{-1}$ yields
 251 $\rho_{CO_2}=0.0281 \text{ g/cm}^3$ using the densimeter of Wang et al. (2019), but $\rho_{CO_2}=0.1397$
 252 g/cm^3 using the densimeter of Kawakami et al. (2003). For a bubble volume of 5%
 253 (the 80th percentile of bubble volume proportions at Kilauea from Tucker et al.,
 254 2019) and a melt density of 2.75 g/cm^3 , these different densimeters predict a con-
 255 tribution of 538 ppm vs. ~ 2674 ppm CO_2 to the reconstructed total CO_2 budget
 256 of the melt inclusion. For a melt inclusion with $SiO_2=49 \text{ wt\%}$, and $H_2O=0.5 \text{ wt\%}$,
 257 these CO_2 contents correspond to entrapment pressures of $\sim 1.2 \text{ kbar}$ vs. 4.8 kbar
 258 (at 1200°C ; Newman & Lowenstern, 2002), and entrapment depths of $\sim 4 \text{ km}$ vs.
 259 $\sim 18 \text{ km}$ respectively for a crustal density of 2700 kg/m^3 . Thus, the development
 260 of an instrument-specific calibration is essential to differentiate between lower and
 261 upper crustal storage at ocean island volcanoes, let alone fingerprinting the involve-
 262 ment of different reservoirs identified by geophysical techniques.

263 An additional source of error affecting both Raman measurements and EOS
 264 methods arises during the conversion of ρ_{CO_2} into the equivalent amount of CO_2 in
 265 ppm held within the vapor bubble ($[CO_2]^{VB}$):

$$[CO_2]^{VB} = 10^6 \times \frac{\rho_{CO_2} V_{VB}}{\rho_{Melt} V_{Melt}} \quad (1)$$

266 Where V_{VB} and V_{Melt} are the volume of the vapor bubble and the melt phase of
 267 the inclusion respectively, and ρ_{Melt} is the density of the silicate melt calculated
 268 here using DensityX (Iacovino & Till, 2019). Total CO_2 contents are obtained by
 269 summing the equivalent amount of CO_2 in the vapor bubble with the concentration
 270 of CO_2 measured in the melt phase ($[CO_2]^{Melt}$) by SIMS or FTIR:

$$[CO_2]^{Tot} = [CO_2]^{VB} + [CO_2]^{Melt} \quad (2)$$

271 The volumes of the vapor bubble and melt inclusion are typically determined
 272 from 2D transmitted light images, estimating the length of the third, unmeasurable

273 dimension from the major and minor axes of the plan view of the inclusion. Tucker
274 et al. (2019) simulate this process by randomly intersecting ellipses and show that
275 the smallest errors are achieved by calculating the third dimension as the arithmetic
276 mean of the two measured axes. However, this approach is still associated with a 1σ
277 error of -47 to +37% (Tucker et al., 2019). Although important, we note that this
278 random error is entirely overwhelmed by the systematic error of up to a factor of 4
279 in literature datasets which have arbitrarily chosen a literature densimeter.

280 To mitigate the systematic error associated with Raman calibration, we de-
281 termine the relationship between Δ and ρ_{CO_2} for the specific instrument and ac-
282 quisition conditions used in this study through the analysis of synthetic fluid melt
283 inclusions with known CO_2 densities. Analysis of both the melt phase (using SIMS)
284 and the vapor bubble (using a calibrated Raman system) yields the first extensive
285 dataset critically evaluating the contribution of vapor bubbles to the total CO_2 bud-
286 get of specific melt inclusions at Kīlauea. Combined with a rigorous examination of
287 the suitability of different CO_2 - H_2O solubility models, these measurements place
288 accurate constraints on entrapment depths of olivine-hosted melt inclusions from the
289 2018 LERZ eruption. This dataset, combined with quantitative models of bubble
290 growth, also allows assessment of the relative importance of post-entrapment crys-
291 tallization and syn-eruptive quenching on the partitioning of CO_2 between the melt
292 and vapor phase. In turn, this allows the accuracy of EOS methods as an alternative
293 to direct measurements of ρ_{CO_2} using Raman Spectroscopy to be evaluated.

294 **3 Materials and Methods**

295 **3.1 Sample Details, Preparation and Analytical Methods**

296 We examine three samples erupted at F8 (square symbols; Fig. 1c):

- 297 1. May-18 (erupted May 30th, 2018; USGS code KE62-3293; blue symbols),
298 comprising vesicular reticulite and scoria which landed in a bucket placed near
299 the F8 vent ($19^\circ 27.7486'$ N, $154^\circ 54.8636'$ W).
- 300 2. July-18 (erupted Mid-July 2018; red symbols), from the selvages of a
301 naturally-quenched, and highly vesicular proximal overflow from the F8 chan-
302 nel (<50 m from the vent; $19^\circ 27.879'$ N, $154^\circ 54.645'$ W).

303 3. Aug-18 (erupted Aug 1st; USGS code KE62-3321F; orange symbols), which
304 was sampled directly from the F8 channel using a metal rod and chain, and
305 rapidly quenched in water. Direct lava sampling took place on a stable chan-
306 nel levee ($19^{\circ} 28.31508' \text{ N}$, $154^{\circ} 54.51426' \text{ W}$), $\sim 700 \text{ m}$ downstream of the
307 position of the July-18 overflow.

308 Samples were jaw crushed and sieved into three size fractions (250–840, 840–
309 1000 and $>1000 \mu\text{m}$). Olivines were picked under a binocular microscope, and in-
310 dividually mounted in CrystalBondTM on glass slides. Care was taken to prepare
311 melt inclusions hosted within olivine crystals from all three size fractions. Melt in-
312 clusions were exposed by grinding with 250–3000 grade wet and dry paper, allowing
313 embayments to be avoided, and melt inclusions containing vapor bubbles to be iden-
314 tified. Melt inclusions without vapor bubbles were ground down with progressively
315 finer wet and dry paper until the center of the inclusion was exposed. Melt inclu-
316 sions containing vapor bubbles were ground down to just above the top of the melt
317 inclusion of interest (to avoid intersecting the bubble, and releasing the trapped
318 CO_2). A photo was taken of the melt inclusion and vapor bubble using a transmit-
319 ted light microscope to allow estimation of melt inclusion and bubble volumes. For
320 larger melt inclusions, two images were acquired: one where the bubble was in focus,
321 and one where the melt inclusion outline was in focus. The outline of the bubble
322 and melt inclusion were traced using ImageJ (Schneider et al., 2012), and a best
323 fit ellipse was fitted to each. Volumes were calculated by assuming that the third
324 (non-measurable dimension) was equal to the arithmetic mean of the two measured
325 dimensions (Tucker et al., 2019). Several melt inclusions contained large spinel crys-
326 tals that were likely co-entrapped. The volume of these spinels (assuming a cuboid
327 shape, with the third dimension also equal to the arithmetic mean of the visible
328 dimensions) was subtracted from the volume of the melt inclusion.

329 Following optical measurements, crystals were ground down until the vapor
330 bubble was within $\sim 30 \mu\text{m}$ of the surface. Depending on the optical quality after
331 fine grinding (using 2000-7000 grade wet and dry paper), melt inclusions were vari-
332 ably polished using $9 \mu\text{m}$ diamond pastes prior to Raman analysis. Raman spectra
333 of vapor bubbles were collected using a confocal LabRAM 300 (Horiba Jobin Yvon)
334 Raman spectrometer in the Department of Earth Sciences at the University of Cam-

335 bridge. Fermi Diads were fitted with Gaussian peaks after subtracting a polynomial
 336 fit to the background (see Supporting Information Fig. S4). The relationship be-
 337 tween Δ and ρ_{CO_2} for the specific Raman acquisition condition used in this study
 338 was determined by analyzing 16 synthetic $CO_2 - H_2O$ fluid inclusions with a range
 339 of densities ($\sim 0.04 \text{ g/cm}^3$, $\sim 0.08 \text{ g/cm}^3$ and $\sim 0.14 \text{ g/cm}^3$) hosted in quartz, as
 340 well as three Kīlauean melt inclusion vapor bubbles. The densities of all 19 of these
 341 primary standards were measured using a JY Horiba LabRam HR in the Fluids Re-
 342 search Laboratory at Virginia Tech Raman, which has been specifically calibrated
 343 for low CO_2 densities using a high-pressure optical cell (Lamadrid et al., 2017). A
 344 linear regression through repeated measurements of standards on the Cambridge
 345 Raman yielded the following relationship with 95% confidence intervals on the re-
 346 gression (see Supporting Information Fig. S3):

$$\rho_{CO_2}(\text{g/cm}^3) = 0.3217 \pm 0.026 \Delta (\text{cm}^{-1}) - 32.995 \pm 2.7 \quad (3)$$

347 Further analytical details are presented in the Supporting Information (Text
 348 S1). Following Raman analyses, individual crystals were ground down to expose the
 349 center of each melt inclusion to maximize the available analyzable area. The bubble
 350 was exposed in approximately half of bubble-bearing inclusions. Following sonication
 351 to remove polishing residue, exposed bubble walls were examined on the FEI Quanta
 352 650FEG SEM at the University of Cambridge in low vacuum mode prior to the ap-
 353 plication of any coatings. Crystals were then mounted in epoxy in groups of 20–40,
 354 and polished with progressively finer diamond pastes (9, 6, 3, 1, $0.25 \mu\text{m}$).

355 Following the application of a gold coat, the concentrations of H_2O and CO_2
 356 (as well as MgO and SiO_2 for normalization) in melt inclusions and co-erupted
 357 matrix glasses were determined using the Cameca IMS-7f GEO at the NERC Ion
 358 Microprobe Facility, University of Edinburgh. SIMS analysis was performed prior to
 359 EPMA analysis to avoid volatile migration under the electron beam, and to avoid
 360 contamination of measured carbon concentrations by a carbon coat. Epoxy stubs
 361 were placed in the sample chamber at vacuum for a minimum of 6 hours before
 362 analysis to allow them to outgas. A wide variety of standards were analyzed to cre-
 363 ate calibration curves for H_2O and CO_2 (N71, M10, 519-4-1, M5, M40, M36, M21,
 364 M47, M36; see Supporting Information S5; Shishkina et al., 2010; Hauri, 2002).

365 Additional information regarding calibration, background and drift corrections are
 366 provided in the Supporting Information (Text S2).

367 Following SIMS analyses, the Au coat was removed by polishing on a 0.25
 368 μm diamond polishing pad, and a carbon coat was applied for EPMA analyses.
 369 Spot analyses of melt inclusions, matrix glasses and host olivines were obtained
 370 using a Cameca SX100 EPMA in the Department of Earth Sciences, University of
 371 Cambridge following the two-condition analytical set up described in Wieser et al.
 372 (2019). Spectrometer configurations, count times, calibration materials, and esti-
 373 mates of precision and accuracy calculated from repeated analyses of secondary
 374 standards (San Carlos Olivine, VG2 and A99; Jarosewich, 2002) are presented in the
 375 Supporting Information (Text S3, Tables S2-4).

376 Melt inclusion compositions were corrected for the effects of post-entrapment
 377 crystallization using the Olivine MI tool in Petrolog3 (Danyushevsky & Plechov,
 378 2011). This requires the user to specify the initial FeO_T and the host Fo content
 379 of each inclusion. FeO_T was set at 11.33 wt% for melt inclusions hosted in olivines
 380 with forsterite contents ($[\text{Fo}=\text{Mg}^{2+}/(\text{Mg}^{2+}+\text{Fe}^{2+}) \text{ atomic}]>79$ mol% based on the
 381 liquid line of descent at Kīlauea, and for consistency with previous studies (Wieser
 382 et al., 2019; Sides, Edmonds, MacLennan, Swanson, & Houghton, 2014). For olivine
 383 crystals with $\text{Fo}<79$ mol%, the initial FeO content was estimated from the relation-
 384 ship between the equilibrium olivine forsterite content and melt FeO_T contents in
 385 a fractional crystallization model computed in MELTS for MATLAB (Supporting
 386 Information Fig. S5 Antoshechkina & Ghiorso, 2018; Gualda et al., 2012).

387 4 Results

388 F8 melt inclusions are hosted in olivine crystals with a wide range of core com-
 389 positions (Fo_{77-89} ; Fig. 2a). Core compositions in all three samples show a peak
 390 at $\sim\text{Fo}_{88-89}$ (Fig. 2b-d), which lies significantly above the equilibrium field cal-
 391 culated from the Mg# of co-erupted matrix glasses [$\text{Mg}\#=\text{Mg}^{2+}/(\text{Mg}^{2+}+\text{Fe}^{2+})$,
 392 atomic], even considering a wide range of experimentally-determined values for
 393 $K_{D_{\text{Fe}^{2+}}^{\text{ol-melt}}}$ (black lines, Fig. 2a; 0.270–0.352; Roeder & Emslie, 1970; Matzen et
 394 al., 2011). Fourteen melt inclusions from May-18, but only six melt inclusions from
 395 July-18 and one from Aug-18 are hosted in olivines which lie within the equilibrium

396 field. F8 olivines have some of the highest Fo contents ever reported at Kīlauea (Fig.
397 2a-d vs. Fig. 2e-f; Sides, Edmonds, Maclennan, Swanson, & Houghton, 2014; Wieser
398 et al., 2019), but relatively low carrier melt Mg#s (51–57 mol%; assuming $\text{Fe}^{3+}/\text{Fe}_T$
399 = 0.15). In turn, this juxtaposition produces some of the most extreme degrees of
400 olivine-carrier melt Fe-Mg disequilibrium seen at Kīlauea (Fig. 2a). Crystals with
401 high forsterite cores show strong normal zoning, while crystals with core composi-
402 tions plotting closer to the equilibrium field on Fig. 2a are not visibly zoned in rapid
403 EDS acquisitions (see Supporting Information Figs. S7-9).

404 The majority of F8 melt inclusions exhibit lower measured FeO_T contents
405 than co-erupted matrix glasses and the composition of Kīlauean melt inclusions
406 from the literature (grey dots; Wieser et al., 2019; Tucker et al., 2019; Sides, Ed-
407 monds, Maclennan, Houghton, et al., 2014; Sides, Edmonds, Maclennan, Swan-
408 son, & Houghton, 2014). Melt inclusion MgO contents are more similar to those of
409 co-erupted matrix glasses (Fig. 3a). Following a correction for the effects of post-
410 entrapment crystallization, F8 melt inclusions have MgO contents between 6.4 and
411 13.7 wt%, and FeO_T contents between 11.3 and 12 wt% (Fig. 3a, Supporting In-
412 formation Fig. S5). Despite the high degree of Mg# disequilibrium between olivine
413 crystals and their carrier melts (Fig. 2a), measured melt inclusion Mg#s (uncor-
414 rected for the effects of PEC) mostly lie within, or close to the equilibrium field
415 calculated from the core compositions of their host olivines (Fig. 3b). The distance
416 from the equilibrium field degree is largest in the July-18 sample, but still smaller
417 than the vast majority of melt inclusions data from other Kīlauean eruptions, par-
418 ticularly those hosted in olivines with higher Fo contents (Fig. 3b). Melt inclusions
419 hosted in olivine crystals which have the highest degree of disequilibrium with their
420 carrier melts (calculated by subtracting the equilibrium Fo content of the co-erupted
421 matrix glass from the Fo content of each olivine) have experienced the most PEC
422 (Fig. 3c) and have the lowest measured FeO_T contents (Fig. 3d).

423 To encapsulate the variable degrees of olivine-melt disequilibrium, and to aid
424 comparisons between different crystal populations, we subdivide F8 olivines into two
425 groups. The first group contains olivines which lie within, or close to the equilib-
426 rium field calculated from the Mg# of the co-erupted matrix glass (Fig. 2a). For
427 the May-18 sample, the division was placed at $\text{Fo}_{81.5}$, based on the near continuous
428 distribution of olivines from slightly above to within the equilibrium field (which can

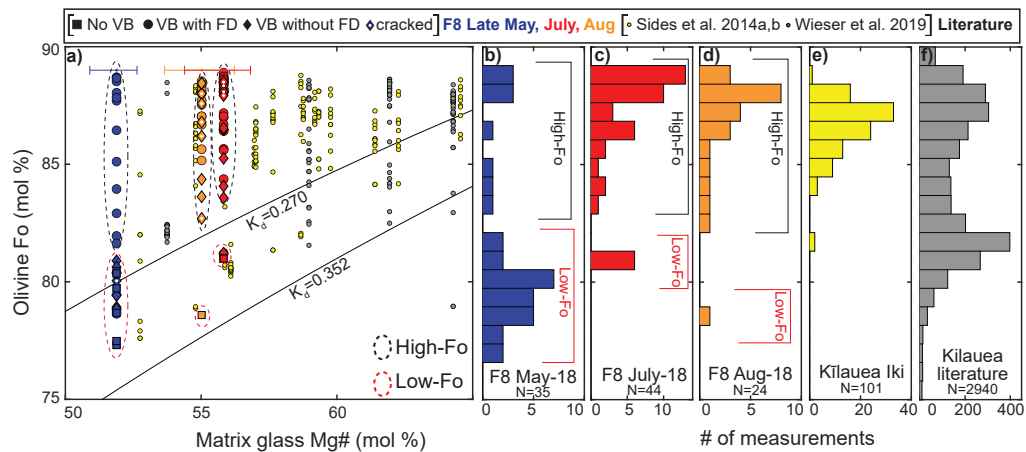


Figure 2. Olivine populations and olivine-melt relationships at F8 compared to literature data. a) Core olivine forsterite content versus matrix glass Mg# for $\text{Fe}^{3+}/\text{Fe}_T=0.15$ (Moussallam et al., 2016; Helz et al., 2017). Olivines lying between the black lines ($K_D=0.270\text{--}0.352$) are in equilibrium with their carrier melts considering the range of experimentally-determined Fe-Mg partition coefficients (Roeder & Emslie, 1970; Matzen et al., 2011). F8 olivines have some of the highest Fo contents observed at Kilauea, yet are hosted in carrier liquids with some of the lowest Mg#s. Literature data from Wieser et al. (2019), Sides, Edmonds, Maclennan, Houghton, et al. (2014), Sides, Edmonds, Maclennan, Swanson, and Houghton (2014). b-d) Histograms of olivine Fo contents from this study, e) Kilauea Iki (Sides, Edmonds, Maclennan, Houghton, et al., 2014; Sides, Edmonds, Maclennan, Swanson, & Houghton, 2014), and f) the compilation of literature analyses presented in Wieser et al. (2019) combined with new measurements from Tucker et al. (2019). The strong bimodality in F8 forsterite contents, along with the degree of olivine-melt disequilibrium was used to subdivide melt inclusions into those hosted within High-Fo olivines (black dotted outline) and Low-Fo olivines (red dotted outline). Olivines are further subdivided into those hosting a melt inclusion without a vapor bubble (no VB), with a vapor bubble which produces a Fermi diad (VB with FD), those with a vapor bubble that does not produce a Fermi diad (VB without FD). Melt inclusions which are cracked, and have a vapor bubble without a FD, are indicated with a white dot.

429 easily be generated by slight cooling between crystallization and eruption), and the
 430 slight gap between these olivines and those with higher Fo contents (Fig 2b). The
 431 second group contains olivines which lie outside the equilibrium field. For brevity,

432 these groups are referred to as Low-Fo and High-Fo olivines, although this classi-
433 fication evaluates the forsterite content of the olivine relative to the Mg# of the
434 co-erupted matrix glass, rather than the absolute Fo content (see Fig. 3c). A sim-
435 ilar classification for the eruptions on Fig. 2 with higher glass Mg#s would place
436 the boundary between groups at higher Fo contents (e.g., the Fo₈₄ division used by
437 Wieser et al., 2019).

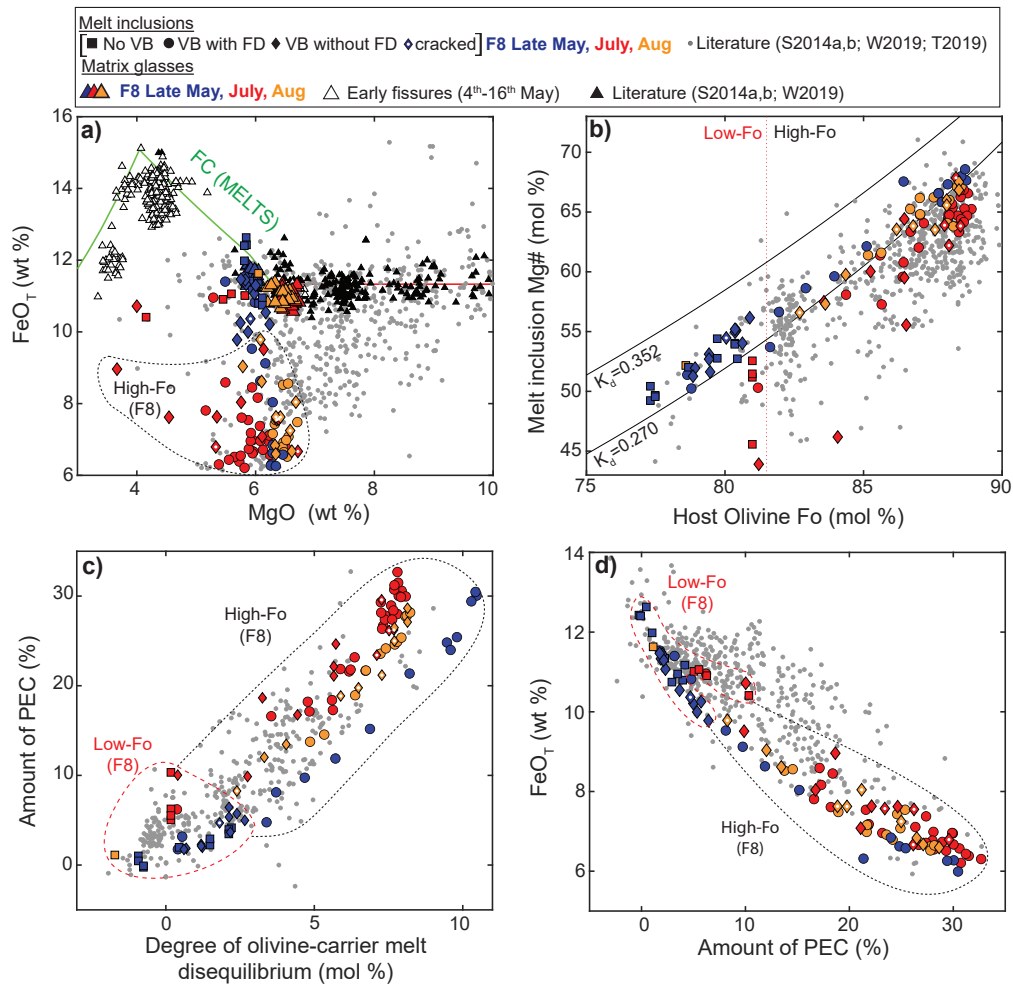


Figure 3. Measured major element systematics for F8 melt inclusions (uncorrected for the effects of PEC). a) High-Fo F8 melt inclusions have significantly lower FeO_T contents than liquid line of descent defined by Kilauean matrix glasses from (this study, Wieser et al., 2019; Sides, Edmonds, MacLennan, Houghton, et al., 2014), and a MELTS for MATLAB (Antoshechkina & Ghiorso, 2018; Gualda et al., 2012) fractionation path following the onset of clinopyroxene and plagioclase fractionation (green line) which recreates glass compositions erupted from earlier, more evolved fissures during the 2018 eruption (4-5 wt% MgO, white triangles). Despite highly variable FeO_T contents, the MgO contents of melt inclusions mostly align with those of their co-erupted matrix glasses. b) In contrast to the prominent disequilibrium between High-Fo olivine compositions and co-erupted matrix glasses (Fig. 1a), melt inclusion Mg#s uncorrected for the effects of PEC (for Fe³⁺/Fe_T=0.15) plot close to the equilibrium field with their host olivines (particularly melt inclusions from the May-18 and Aug-18 samples). Melt inclusions from previous Kilauean eruptions (Wieser et al., 2019; Tucker et al., 2019; Sides, Edmonds, MacLennan, Houghton, et al., 2014; Sides, Edmonds, MacLennan, Swanson, & Houghton, 2014, grey dots) lie much further below the equilibrium field. c) The amount of PEC (calculated in Petrolog3; Danyushevsky & Plechov, 2011) is strongly correlated with the degree of ol-melt disequilibrium, calculated by subtracting the equilibrium olivine composition of the co-erupted matrix glass (for K_D=0.3) from the measured Fo content. d) The FeO_T contents of F8 melt inclusions also shows a strong negative correlation with the amount of PEC, extending to lower values than the vast

438 All High-Fo melt inclusions contain a vapor bubble (Fig. 3c), 73% (N=53) of
439 which produce a Fermi diad (FD) during Raman analysis. Vapor bubbles which do
440 not produce a FD may contain no CO₂, or CO₂ densities below the detection limit
441 of Raman spectroscopy. While the detection limit will depend on the exact depth
442 of the bubble below the surface, as well as the transparency of the host crystal, the
443 distribution of densities in vapor bubbles which produced a FD indicates that the
444 detection limit lies between 0–0.02 g/cm³ (light green bar in Fig. 4c). Nine of the
445 bubbles without a FD are hosted within cracked melt inclusions, which may have
446 resulted in CO₂ loss from the bubble (diamonds with white dots; Fig. 3 and 4, see
447 Supporting Information Fig. S10 Aster et al., 2016). In contrast, only 50% (N=15)
448 of Low-Fo melt inclusions contain a vapor bubble, and only 20% (N=3) of these pro-
449 duce a FD (Fig. 3c). Only 1 of the bubbles without a FD is hosted within a cracked
450 melt inclusion.

451 Bubble-bearing melt inclusions show a correlation between the volume % of
452 the bubble and the amount of PEC, despite the large random errors associated with
453 measuring bubble proportions from 2D images (grey error bars; Fig. 4a). There is
454 a substantial drop in glass CO₂ contents with increasing PEC, and melt inclusions
455 containing vapor bubbles with a FD show significantly lower glass CO₂ contents
456 than bubble-free melt inclusions (Fig. 4b, $p=10^{-7}$; Kolmogorov Smirnov test).
457 There is no obvious correlation between the CO₂ density in vapor bubbles and the
458 amount of PEC (Fig. 4c, $R^2=10^{-5}$), the CO₂ density and the glass CO₂ content
459 ($R^2=0.1$) or the CO₂ density and the volume of the bubble ($R^2=0.0004$). The me-
460 dian and mean proportion of the total melt inclusion CO₂ budget hosted within the
461 bubble is 93% and 87% respectively (black histogram; Fig. 4d). This exceeds the
462 proportions calculated by Moore et al. (2015) for melt inclusions from the 1959 and
463 1960 eruptions of Kīlauea (median=67%, mean=65%; blue histogram). This dis-
464 crepancy reflects the fact that Moore et al. (2015) did not measure the CO₂ content
465 of the glass in each melt inclusion, so they calculated proportions assuming a glass
466 CO₂ content of 300 ppm (the maximum measured in the same suite of samples by
467 Tuohy et al., 2016). Our new data shows the importance of measuring CO₂ in the
468 glass and bubble of a specific melt inclusion; while bubble-free melt inclusions have
469 CO₂ contents up to 417 ppm in the glass phase, those with vapor bubbles produc-
470 ing a FD have median CO₂ contents of only 45 ppm (mean=54 ppm; Fig. 4b). In

471 contrast to the highly variable CO₂ contents in melt inclusion glasses, H₂O contents
472 are remarkably constant within a given eruption, despite significant variation in the
473 contents of incompatible elements such as Na₂O and K₂O (Fig. 5a). Excluding two
474 degassed melt inclusions (~ 0.09 wt% H₂O), F8 melt inclusions have between 0.19–
475 0.33 wt% H₂O, which is lower than most of the Kīlauean melt inclusions measured
476 by Sides, Edmonds, MacLennan, Houghton, et al. (2014); Sides, Edmonds, MacLen-
477 nan, Swanson, and Houghton (2014) and almost all of those measured by Tucker et
478 al. (2019) (Fig. 5b).

479 5 Discussion

480 5.1 Mineral-melt disequilibrium drives the growth of a CO₂-rich 481 bubble

482 The prominent Mg# disequilibrium between the core compositions of High-Fo
483 olivines from F8 and their carrier melts has been observed in a number of historic
484 eruptions at Kīlauea (Fig. 2; Tuohy et al., 2016; Wieser et al., 2019; Sides, Ed-
485 monds, MacLennan, Houghton, et al., 2014; Sides, Edmonds, MacLennan, Swanson, &
486 Houghton, 2014). Based on major and trace element disequilibrium between melt in-
487 clusions and their carrier melts (e.g., Nb/Y ratios), as well as microstructures consis-
488 tent with deformation of the crystal lattice (also observed in some High-Fo olivines
489 from F8 by Gansecki et al., 2019), Wieser, Edmonds, et al. (2020) and Wieser et
490 al. (2019) suggested that highly forsteritic olivines are scavenged from long-lived
491 plastically-deforming mush piles at the base of the SC reservoir, and incorporated
492 into cooler, lower Mg# carrier melts with different trace element signatures just
493 prior to eruption. These studies also suggest that olivines with lower forsterite con-
494 tents exhibiting small amounts of olivine-melt disequilibrium (similar to the Low-Fo
495 olivines in this study), no lattice distortions, and a high degree of trace element
496 equilibrium may have crystallized from their carrier melts as true phenocrysts. The
497 distinct populations of high- and low-Fo olivines examined here may have similar
498 origins.

499 Kīlauean melts with greater than ~ 6.8 wt% MgO are saturated in only olivine
500 and minor chrome-spinel (Wright & Fiske, 1971), so show a strong correlation be-
501 tween temperature and the MgO content of the melt (Helz & Thornber, 1987). The

502 remarkably constant FeO contents of high MgO Kīlauean melts (Fig. 3a) means that
503 glass Mg# is strongly correlated with MgO, and therefore temperature. As glass
504 Mg# is closely related to the olivine forsterite content through the Fe-Mg olivine-
505 liquid exchange coefficient, equilibrium olivine forsterite contents are also strongly
506 correlated with temperature. Thus, the difference in Mg# between the measured
507 olivine core composition, and the equilibrium olivine forsterite content calculated
508 from the composition of co-erupted matrix glasses (termed the degree of olivine-melt
509 disequilibrium) is proportional to the amount of cooling experienced by the inclu-
510 sion prior to syn-eruptive quenching (Wieser et al., 2019). The close relationship
511 between the amount of cooling experienced by an inclusion, and the amount of PEC
512 (Danyushevsky et al., 2000) accounts for the excellent correlation between the degree
513 of olivine-melt disequilibrium and the amount of PEC (Fig. 3c).

514 F8 melt inclusions are hosted in some of the most forsteritic olivines erupted
515 at Kīlauea, yet were erupted in carrier melts with some of the lowest Mg#s (Fig.
516 2a). Consequently, they have experienced some of the largest amounts of cooling
517 following entrapment, and, by extension, some of the largest amounts of PEC ever
518 reported at Kīlauea (up to $\sim 33\%$; Fig. 3c), see also Lerner (2020) and Lerner et al.
519 (2020). These PEC extents are also significantly larger than those reported from
520 other volcanic systems; olivine-hosted melt inclusions from Holuhraun (Iceland),
521 Piton de la Fournaise (Réunion) and Erebus (Antarctica) have experienced $\sim 5\%$,
522 $< 12\%$ and $0\text{--}4.2\%$ PEC respectively (Hartley et al., 2015; Collins et al., 2012; Mous-
523 sallam et al., 2014). The small amounts of cooling (and therefore PEC) experienced
524 by Low-Fo olivines, which are close to equilibrium with their carrier melts, likely
525 occurred during fractionation between the formation and eruption of these crystals
526 (Fig. 3c). However, progressive fractionation and cooling of a batch of melt can-
527 not account for the peak at $\sim \text{Fo}_{88-89}$ in F8 samples (Wieser et al., 2019; Maaløe
528 et al., 1988), nor the paucity of olivines with Fo contents in equilibrium with the
529 co-erupted matrix glasses (particularly in the July and Aug samples; Fig. 2a). Based
530 on the similarities between the High-Fo olivines from F8 and previous studies (large
531 amounts of olivine-melt disequilibrium, presence of lattice distortions; Gansecki et
532 al., 2019), we appeal to the process proposed by Wieser et al. (2019), where cooling
533 is not a gradual process during progressive differentiation of a given magma batch
534 (Maaløe et al., 1988), but occurs over short timescales, when High-Fo olivine crys-

535 tals residing in hot mush piles are mixed into significantly cooler, lower Mg# melts
536 (Wieser et al., 2019; Sides, Edmonds, MacLennan, Houghton, et al., 2014), see also
537 Shea et al. (2019).

538 Melt inclusion MgO and FeO_T contents are strongly affected by the crystal-
539 lization of olivine on the walls of the melt inclusion (PEC), and subsequent diffusive
540 re-equilibration. Based on the strong coupling between MgO content and tempera-
541 ture in olivine-saturated liquids (Helz & Thornber, 1987), thermal equilibration of
542 a hot olivine crystal with a cooler carrier melt drives the crystallization of a zoned
543 olivine rim from the melt inclusion, causing the MgO content of the melt inclusion
544 to drop to match that of the carrier melt (Fig. 3a). This zoned olivine rim begins to
545 re-equilibrate with the host crystal, and, in turn, the melt inclusion re-equilibrates
546 with the changing rim composition (Danyushevsky et al., 2000). The melt inclusion
547 loses FeO by diffusion to achieve Mg# equilibration with the host olivine follow-
548 ing the large initial drop in MgO during cooling. As the MgO content of the melt
549 inclusion is a function of the temperature, FeO diffusion is countered by MgO dif-
550 fusion in the opposite direction, which is sequestered by further post-entrapment
551 crystallization of olivine on the wall of the melt inclusion.

552 This FeO-loss process accounts for the negative correlation between melt in-
553 clusion FeO_T contents and the amount of PEC (Fig. 3d). For a given amount of
554 PEC, F8 melt inclusions have lower FeO_T contents and display a smaller degree
555 of Mg# disequilibrium with their olivine host than the vast majority of literature
556 data (Fig. 3b, d). It is important to note that methods calculating the amount of
557 PEC based on the degree of Mg# disequilibrium between the melt inclusion and the
558 host crystal (e.g., Tucker et al., 2019; Neave et al., 2017) will significantly under-
559 estimate the true amount of PEC in melt inclusions where extensive FeO-loss has
560 occurred compared to the Petrolog3 method used here where the user specifies an
561 initial FeO_T content. For example, the May-18 melt inclusions with $\text{Fo} > 85$ have lost
562 sufficient quantities of FeO by diffusive re-equilibration such that their Mg#s are in
563 equilibrium with the composition of the host olivine. Thus, methods based on Mg#
564 comparisons would indicate that these melt inclusions have experienced very minor
565 amounts of PEC. However, their FeO contents lie ~ 4 wt% below the composition
566 of co-erupted matrix glasses, indicating that their compositions have been heavily
567 altered by the PEC process (Fig. 3a).

568 The higher degrees of diffusive FeO-loss for a given amount of PEC for F8
 569 melt inclusions compared to literature data (Fig. 3d) indicates that there was a
 570 longer time lag between the entrainment of crystals into cooler melts and their
 571 eventual eruption. Danyushevsky et al. (2002) quantitatively model Fe-Mg re-
 572 equilibration to estimate this time lag: their Fig. 4c shows that a melt inclusion
 573 with a $\sim 50 \mu\text{m}$ radius that has experienced $\Delta T=100\text{--}150^\circ\text{C}$ and undergone FeO loss
 574 at $T=1150\text{--}1200^\circ\text{C}$ achieves 98% equilibrium in ~ 2 years. These extents of cooling
 575 and temperatures of re-equilibration are representative of F8 inclusions. However,
 576 Danyushevsky et al. (2002) assume isotropic diffusion of Fe through the host olivine
 577 crystal with $D_{\text{Fe, Mg}} \sim 3\text{--}6 \times 10^{-17} \text{ m}^2/\text{s}$ at $1150\text{--}1200^\circ\text{C}$. In reality, FeO loss will be
 578 dominated by diffusion along the fast c-direction in olivine ($D_{\text{Fe, Mg}} \sim 1\text{--}4 \times 10^{-16}$
 579 m^2/s for $\text{Fo}_{80\text{--}89}$, $T=1150\text{--}1200^\circ\text{C}$, and QFM to QFM+0.3; Chakraborty, 2010;
 580 Barth et al., 2019). Thus, complete re-equilibration could be achieved almost an
 581 order of magnitude faster, in a matter of months. Considering the substantial un-
 582 certainties in this method associated with the fact the model of Danyushevsky et
 583 al. (2002) does not account for diffusional anisotropy, and the fact the degree of
 584 re-equilibration is very sensitive to the choice of K_D (Fig. 3b), the FeO_T system-
 585 atics of melt inclusions within High-Fo olivines erupted on May 28th ($\sim 70\text{--}100\%$
 586 re-equilibration) indicate that entrainment into cooler carrier melts occurred approx-
 587 imately a month to a year prior to eruption.

588 5.2 Diffusive H_2O -loss

589 Given that H_2O in melt inclusions diffusively re-equilibrates over hours to days
 590 (Hartley et al., 2015; Le Voyer et al., 2014; Gaetani et al., 2012), the timescales in-
 591 ferred from Fe-Mg disequilibrium are more than sufficient for H_2O contents within
 592 F8 melt inclusions to be fully reset to the H_2O content of the melt which carried
 593 them to the site of the eruption. This re-equilibration accounts for the remarkably
 594 uniform H_2O contents of F8 melt inclusions in each sample, despite substantial
 595 variation in the concentration of other incompatible elements (e.g., Na_2O ; Fig. 5a).
 596 The approximately constant H_2O contents in melt inclusions from each sample in-
 597 dicates that F8 carrier melts erupted in late May had H_2O contents of 0.29 wt%,
 598 while those erupted in July and August had slightly lower H_2O contents ($\sim 0.22\text{--}0.23$
 599 wt%). These carrier melts are relatively H_2O -poor compared to the composition

600 of previously-erupted Kilauean melts (inferred from published melt inclusion data;
601 Fig. 5). The presence of more H₂O-poor carrier melts in 2018 likely results from the
602 extensive mixing of magmas which had partially degassed their H₂O at the summit
603 lava lake with undegassed melts within the plumbing system between 2008 and 2018
604 (see also Lerner, 2020). This is similar to the mechanism proposed for the variable
605 volatile contents of Puna Ridge magmas by Dixon (1991) degassing.

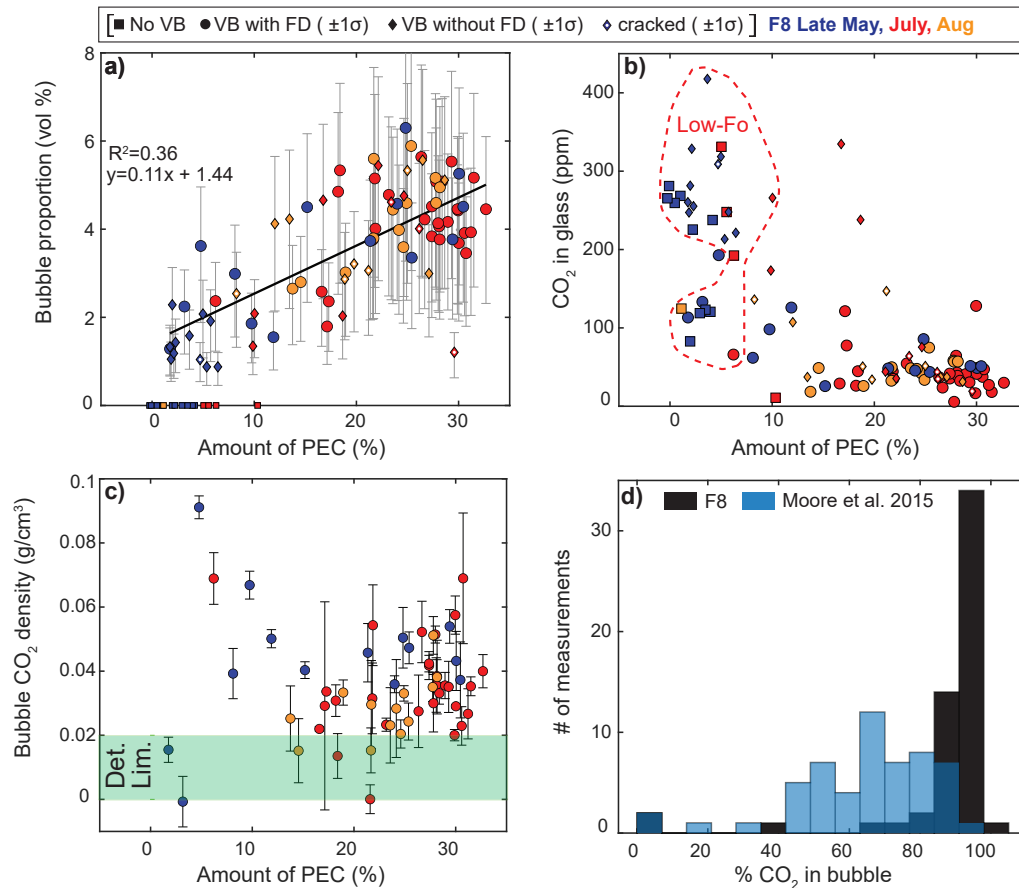


Figure 4. Vapor bubble and melt inclusion CO₂ systematics. a) There is a positive correlation between the volume proportion of the vapor bubble (VB) and the amount of PEC. Only melt inclusions which have experienced <10% PEC are bubble-free. Error bars show the 1σ errors associated with estimating bubble volume proportions from 2D images (-45% and +37% Tucker et al., 2019). b) With increasing amounts of PEC, the amount of CO₂ within the glass phase of the melt inclusion declines. The highest glass CO₂ contents are observed in melt inclusions with no vapor bubbles (squares), and melt inclusion with bubbles that did not produce a FD (diamonds). In contrast, the vast majority of melt inclusions with low glass CO₂ contents have vapor bubbles which produced a FD (circles), or vapor bubbles without a FD that were hosted within cracked melt inclusions (diamonds with white dots). c) There is no correlation between the CO₂ density in vapor bubble measured using Raman Spectroscopy and the amount of PEC. Error bars show the $\pm 1\sigma$ deviation of three repeated measurements of each vapor bubble. The green bar shows our estimate of the detection limit (Det. Lim.) of Raman analyses based on the distribution of measured bubble densities. d) The black histogram shows the proportion of CO₂ held within the vapor bubble for F8 melt inclusions that produced a FD (mean=87%, median=93%). Estimates by Moore et al. (2015) for Kīlauean melt inclusions from the 1959 and 1960 eruptions are also shown.

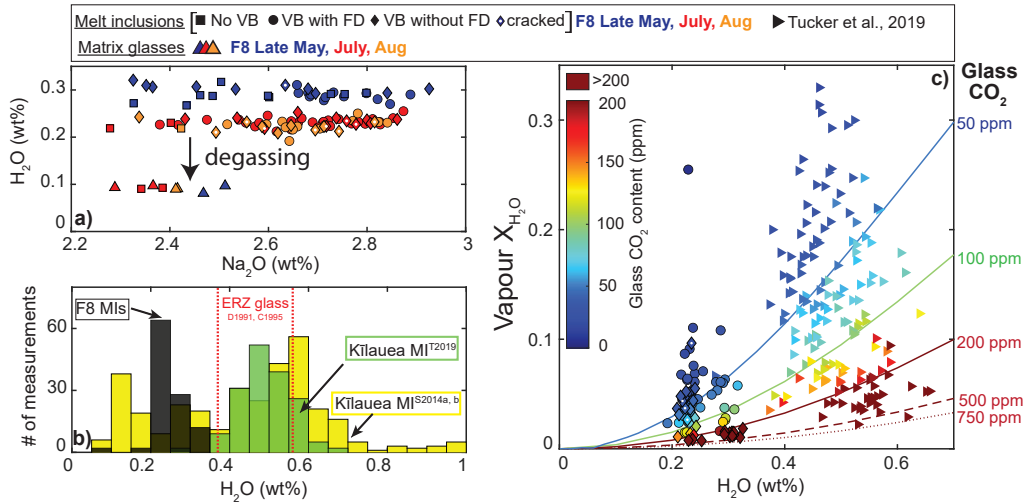


Figure 5. H₂O systematics of F8 melt inclusions relative to literature data from Kilauea. a) F8 melt inclusion H₂O contents are remarkably constant within each sample, despite substantial variations in Na₂O. This indicates that melt inclusion H₂O contents were reset by diffusive re-equilibration with their carrier liquid. The precision of SIMS measurements ($\pm 1.5\%$) is smaller than the symbol size, so error bars are not shown. b) F8 melt inclusions have lower H₂O contents than the majority of Kilauean melt inclusions measured by Sides, Edmonds, Maclennan, Swanson, and Houghton (2014); Sides, Edmonds, Maclennan, Houghton, et al. (2014) (yellow histogram) and almost all of the melt inclusions measured by Tucker et al. (2019). H₂O contents from submarine ERZ glasses with 7–16 wt% MgO from Dixon et al. (1991); Clague et al. (1995) are shown with red dashed lines. c) Relationship between the molar fraction of H₂O in the vapor phase (X_{H_2O}) and the melt H₂O content for five different melt CO₂ contents (50, 100, 200, 500 and 750 ppm; using VolatileCalc-Basalt; Newman and Lowenstern, 2002). X_{H_2O} ratios for the co-existing vapor in equilibrium with the measured concentration of CO₂ and H₂O in the melt phase of the bubble-bearing inclusions from this study and Tucker et al. (2019) (triangles) are overlain, with symbols colored by the CO₂ content of the glass phase. The relatively low H₂O contents of F8 melt inclusions mean that X_{H_2O} is generally < 0.1 . However, a number of inclusions from Tucker et al. (2019) with glass CO₂ contents < 100 ppm have much higher X_{H_2O} ratios. This causes the CO₂ densities predicted using the EOS method to fall below the trend line defined by F8 melt inclusions on Fig. 8a.

5.3 PEC and melt-vapor CO₂ partitioning

It is well recognized that extensive PEC drives the growth of a CO₂-rich vapor bubble (Steele-Macinnis et al., 2011; Sides, Edmonds, MacLennan, Houghton, et al., 2014; Sides, Edmonds, MacLennan, Swanson, & Houghton, 2014; Aster et al., 2016; MacLennan, 2017). Thus, studies measuring only the CO₂ in the melt phase using SIMS or FTIR will yield spuriously low entrapment depths for melt inclusions which have undergone extensive PEC (e.g., Sides, Edmonds, MacLennan, Houghton, et al., 2014). Our concurrent measurements of CO₂ in the melt and bubble phase of a large number of melt inclusions which have experienced a wide range of PEC amounts (Fig. 3c-d) provides a unique opportunity to interrogate the various processes causing CO₂ to partition into the vapor bubble.

To investigate the effects of compositional changes in the melt inclusion associated with PEC, we use the CO₂ solubility model of Shishkina et al. (2014):

$$\ln[\text{CO}_2] = 1.15\ln(P) + 6.71\Pi^* - 1.345 \quad (4)$$

Where [CO₂] is the concentration of CO₂ in ppm, and P is the pressure in MPa. The Π^* term accounts for the compositional dependence on CO₂ solubility, expressed in terms of the cation fractions of 7 major element species:

$$\Pi^* = \frac{\text{Ca}^{2+} + 0.8\text{K}^+ + 0.7\text{Na}^+ + 0.4\text{Mg}^{2+} + 0.4\text{Fe}^{2+}}{\text{Si}^{4+} + \text{Al}^{3+}} \quad (5)$$

We calculate the change in Π^* during PEC, $\Delta \Pi^*$, by subtracting the Π^* value of the PEC-corrected major element composition of each melt inclusion from the Π^* value of the measured composition. $\Delta \Pi^*$ becomes progressively more negative with increasing amounts of PEC, showing that CO₂ becomes progressively less soluble (red dots; Fig. 6b, see also MacLennan, 2017). Changes in Π^* are dominated by a decrease in X_{Mg} , and increase in X_{Si} and X_{Al} resulting from the crystallization of olivine on the walls of the inclusion. These changes are partially counteracted by an increase in X_{Ca} (as Ca is incompatible in olivine). To quantify the magnitude of this drop in Π^* in terms of CO₂ partitioning between the melt and bubble, we consider the 8 melt inclusions which have experienced >30% PEC (all of which contain bubbles which produce a FD). The mean Π^* value of the measured compositions of

633 these melt inclusions is 0.33, while the mean Π^* of their PEC-corrected compositions
634 is 0.39 ($\Delta \Pi^* = -0.068$). For $P = 0.76$ kbar, which is the average entrapment pressure
635 for the PEC-corrected compositions of these melt inclusions calculated using equa-
636 tion 4, CO_2 solubility drops by ~ 192 ppm. As melts at Kīlauea are CO_2 saturated
637 at crustal storage depths (Gerlach et al., 2002), this extra CO_2 will partition into
638 the vapor bubble.

639 However, the mean amount of CO_2 sequestered within the vapor bubbles of
640 these 8 melt inclusions is 657 ± 231 ppm (calculated using equation 1). This reflects
641 three additional processes which enhance CO_2 partitioning into the bubble during
642 PEC. Firstly, the crystallization of olivine, which contains negligible quantities of
643 CO_2 , drives up the total concentration of the CO_2 in the remaining melt by a factor
644 of 1 plus the amount of PEC (1.3 to $1.33\times$ for these 8 melt inclusions). As men-
645 tioned above, because Kīlauea melt inclusions are CO_2 saturated (Gerlach et al.,
646 2002), this excess partitions into the bubble (mean 145 ppm, up to 230 ppm CO_2).
647 Secondly, the preferential contraction of the melt phase relative to the olivine dur-
648 ing thermal re-equilibration leads to a reduction in the volume of the melt phase.
649 This volume reduction is enhanced by the third process; the crystallization of denser
650 olivine on the rim of the melt inclusion. A drop in the internal pressure of the melt
651 inclusion causes the CO_2 solubility to decrease further, driving more CO_2 into the
652 vapor bubble (equation 5). Evidence for these volume changes is provided by the
653 correlation between the amount of PEC and the volume of the vapor bubble (Fig.
654 4a), as well as the observation that all melt inclusions without a vapor bubble have
655 experienced $< 10\%$ PEC (Fig. 4a), while all melt inclusions that have experienced
656 $> 10\%$ PEC have a vapor bubble.

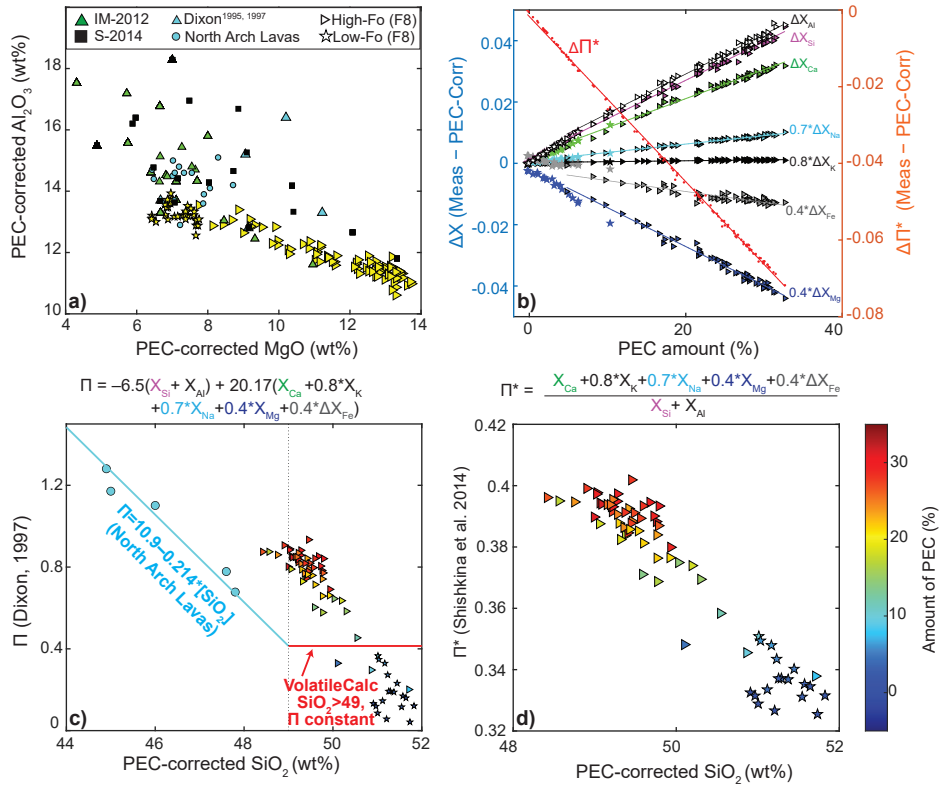


Figure 6. Evaluating the compositional sensitivity of CO₂ solubility. a) Comparison of the MgO vs. Al₂O₃ systematics of PEC-corrected F8 inclusions to the glass compositions used to calibrate each solubility model. The North Arch lavas which define the simplified Π vs. SiO₂ relationship presented in Dixon (1997) and implemented in VolatileCalc-Basalt (Newman & Lowenstern, 2002) are also shown (blue circles). The MagmaSat dataset (Ghiorso & Gualda, 2015) includes the experiments in the calibration datasets of Shishkina et al. (2014), Iacono-Marziano et al. (2012) and Dixon et al. (1995) (so is not shown, as it would cover all these symbols). b) ΔX (triangle and star symbols) and ΔΠ* (red dots Shishkina et al., 2014) for F8 melt inclusions plotted against the amount of PEC. ΔX and ΔΠ* were calculated by subtracting the values of X and Π* for PEC-corrected melt inclusions from the values of X and Π* for measured compositions. For example, inclusion LL8.156 has experienced 33% PEC, and has a PEC-corrected MgO content of 13.5 wt% and a measured MgO content of 5.4 wt%. Thus, ΔX_{MgO} is strongly negative. c) The compositional parameter Π of Dixon (1997) calculated for PEC-corrected F8 melt inclusion compositions varies substantially with SiO₂, following an offset trend to that defined by North Arch Glasses (Dixon et al., 1997, blue dots and linear regression). VolatileCalc-Basalt effectively treats all melt inclusions with >49 wt% SiO₂ as if Π is constant (red line). d) The compositional parameter Π* from Shishkina et al. (2014), and therefore the solubility of CO₂, is significantly higher for High-Fo melt inclusions (which have the highest PEC-corrected MgO, and lowest SiO₂ and Al₂O₃ contents). The color of the symbols for F8 melt inclusions in c) and d) represents the amount of PEC.

657 Overall, changes in melt chemistry, the incompatible behaviour of CO₂, and a
658 drop in the internal pressure of the melt inclusion accounts for the rapid decrease in
659 glass CO₂ contents with increasing PEC (Fig. 4b). Our concurrent measurements of
660 glass and bubble CO₂ provide the first opportunity to see through these convoluting
661 effects of PEC to robustly determine total CO₂ contents, and therefore entrapment
662 depths of Kīlauean melt inclusions. To account for the uncertainty regarding the
663 amount of CO₂ held within bubbles that did not produce a FD (diamond symbols),
664 particularly those hosted within cracked olivines (diamond symbols with white dot),
665 we only calculate total CO₂ contents and entrapment depths for melt inclusions
666 which had no bubble, or a bubble that produced a FD. These total CO₂ were cor-
667 rected for the incompatible behaviour of CO₂ during PEC to determine the total
668 CO₂ content at the point of melt inclusion entrapment.

669 Total PEC-corrected CO₂ contents in melt inclusions hosted within High-Fo
670 olivines are offset to significantly higher values compared to those hosted within
671 Low-Fo olivines (Fig. 7a), indicating that these two olivine populations crystal-
672 lized at distinct depths within Kīlauea’s plumbing system. It is also interesting to
673 compare our total CO₂ contents to previously published data on Kīlauean melt
674 inclusions. Although these studies investigate products from different eruptions,
675 the apparent stability in the geometry of Kīlauea’s plumbing system since at least
676 the 1950s (Helz et al., 2014; Poland et al., 2015; Eaton & Murata, 1960) means
677 such comparisons are still useful (and particularly relevant for studies of the 1959–
678 1960 eruptive period, where activity at the summit was followed by a large LERZ
679 eruption; e.g., Tuohy et al., 2016; Moore et al., 2015; Sides, Edmonds, Maclen-
680 nan, Houghton, et al., 2014; Sides, Edmonds, Maclennan, Swanson, & Houghton,
681 2014) . Unsurprisingly given our findings that ~90% of CO₂ is held within the va-
682 por bubble (Fig. 4d), CO₂ contents in F8 melt inclusions are significantly higher
683 than measurements of just the glass phase by Sides, Edmonds, Maclennan, Swanson,
684 and Houghton (2014); Sides, Edmonds, Maclennan, Houghton, et al. (2014) (Fig.
685 7c). F8 melt inclusions are also offset to higher CO₂ contents than experimentally-
686 rehomogenized melt inclusions (Tuohy et al., 2016, Fig. 7d). Tuohy et al. (2016)
687 note similar offsets between their measurements and Raman reconstructions of bub-
688 ble CO₂ by Moore et al. (2015) in the same sample set. They suggest that their
689 analyses may have been biased towards melt inclusions with smaller bubbles that

690 fully disappear upon heating, lower pressure inclusions that do not fracture during
691 heating, and larger inclusions that can be analysed by FTIR.

692 Interestingly, our distribution of total CO₂ contents for melt inclusions which
693 possessed bubbles are indistinguishable using the Kolmogorov-Smirnov (KS) test
694 (p=0.1) from the CO₂ contribution of just the vapor bubbles in melt inclusions
695 from the 1959 and 1960 eruptions of Kilauea (Moore et al., 2015, Fig. 7e). This
696 demonstrates that in olivine populations which have experienced extensive PEC,
697 measurements of glass CO₂ contents are of subordinate importance to measurements
698 of bubble CO₂. Furthermore, the contribution of CO₂ from the melt phase for the
699 majority of High-Fo melt inclusions from F8 is entirely overwhelmed by the errors
700 on the amount of CO₂ in the bubble associated with estimating bubble volume pro-
701 portions from 2D images. However, it is worth noting that only measuring CO₂ in
702 vapor bubble would have failed to identify the population of Low-Fo olivines which
703 host almost all of their CO₂ within the glass phase. Thus, we suggest that future
704 studies use a small number of SIMS or FTIR analyses of melt inclusions, combined
705 with EPMA analyses of host crystals and melt inclusions, to determine the relation-
706 ship between glass and bubble CO₂ contents and the amount of PEC in different
707 subpopulations of melt inclusions. If the vast majority of CO₂ in a given population
708 is held in the vapor bubble, a limited analytical budget would be better spent accu-
709 rately measuring bubble volumes (using MicroCT or 3D Raman mapping; Pamukcu
710 et al., 2013; Venugopal et al., 2020) to combine with Raman measurements of CO₂
711 density in the rest of the sample set, instead of precisely quantifying the insignificant
712 amount of CO₂ held within the glass phase using SIMS or FTIR.

713 Importantly, we also observe that the distribution of total CO₂ contents in
714 bubble-bearing melt inclusions is significantly higher than bubble-free melt inclu-
715 sions (Fig. 7b). This result invalidates the approach of preferentially targeting
716 bubble-free melt inclusions to avoid having to account for CO₂ within the vapor
717 bubbles (e.g., Helo et al., 2011; Esposito et al., 2011) in systems where erupted crys-
718 tals have experienced extensive PEC prior to eruption. Crucially, analysis of only
719 bubble-free melt inclusions by SIMS or FTIR, or analyses of just vapor bubbles us-
720 ing Raman, would have failed to identify that crystals are supplied from two distinct
721 storage regions within Kilauea's plumbing system.

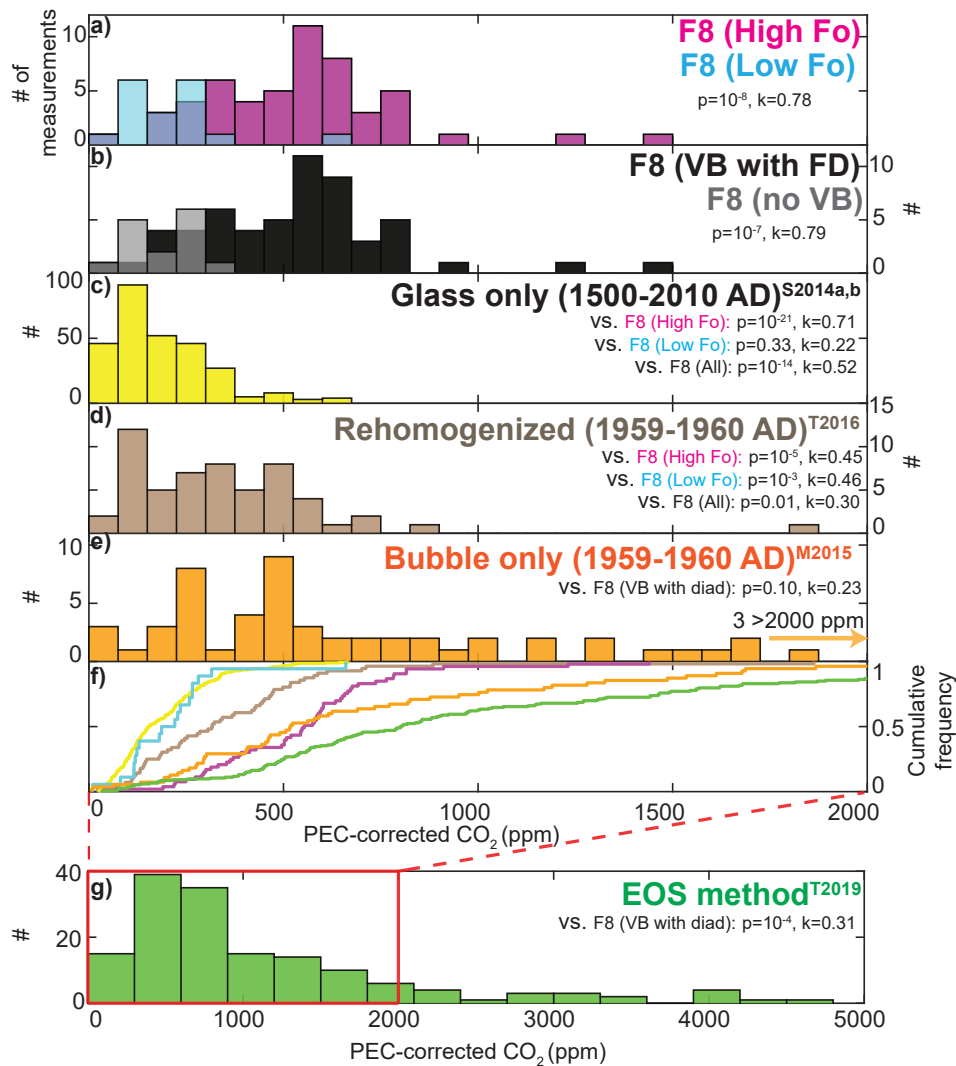


Figure 7.

722 **Caption Fig. 7** Histograms of melt inclusion CO₂ contents from this study and
 723 the literature (all corrected for the effects of PEC). a) Total CO₂ contents (bub-
 724 ble+glass) for High and Low-Fo melt inclusions are statistically distinguishable at
 725 $p=0.05$ using the Kolmogorov Smirnov (KS) test (p value and test statistic k shown
 726 on the figure). b) Similarly, melt inclusions which contain a vapor bubble (VB) with
 727 a FD have significantly higher total CO₂ contents than bubble-free melt inclusions.
 728 c) Melt inclusion CO₂ contents from a suite of eruptions at Kilauea between 1500
 729 and 2008 AD where only the glass phase was measured (Sides, Edmonds, Maclennan,
 730 Swanson, & Houghton, 2014; Sides, Edmonds, Maclennan, Houghton, et al.,
 731 2014). d) CO₂ contents of experimentally-homogenized melt inclusions from the

1959 Kīlauea Iki and 1960 Kapoho eruptions (Tuohy et al., 2016). e) Bubble CO₂ contents from Moore et al. (2015) in the same suite of samples as in d). For consistency, these bubble CO₂ contents were corrected for PEC using the average amount of PEC reported by Tuohy et al. (2016) (13%). f) Cumulative distribution plots for these datasets. g) Total inclusion CO₂ contents from Tucker et al. (2019) where the contribution from bubble CO₂ was estimated using the EOS method (excluding inclusions with bubble volumes >8% that the authors suggest were co-entrapped). 35 melt inclusions have CO₂ >1500 ppm. Note the change in x axis scale from plots a-f). For literature data, all melt inclusions are shown, as Fo contents were not reported by Moore et al. (2015), and matrix glass Mg#s were not reported in Tucker et al. (2019), so it was not possible to classify data based on the degree of olivine-melt disequilibrium as for F8 samples.

5.4 Analytical versus theoretical constructions of vapor bubble CO₂

In contrast to the good agreement between our estimates of total CO₂ contents from combined SIMS and Raman measurements from F8 and the bubble-only measurements of Moore et al. (2015), the total CO₂ contents estimated by Tucker et al. (2019) for a range of Kīlauean eruptions using the EOS method are displaced to significantly higher values (Fig. 7g). To assess the cause of this discrepancy, we follow the EOS method they describe to calculate CO₂ bubble densities for F8 melt inclusions to compare to our Raman measurements. The simplification of the Dixon (1997) solubility model implemented in the excel workbook VolatileCalc (hereafter VolatileCalc-Basalt Newman & Lowenstern, 2002) was used to calculate the internal pressure of the melt inclusion based on the measured SiO₂, CO₂ and H₂O contents of the glass phase. The pure CO₂ EOS of Span and Wagner (1996) implemented in Python3 through CoolProp (Bell et al., 2014) was used to calculate the CO₂ density at this internal pressure and 725 °C, which was the presumed glass transition temperature of Tucker et al. (2019) based on Ryan and Sammis (1981). The Duan and Zhang (2006) EOS utilized by Tucker et al. (2019) yields identical densities to the fourth decimal place (see Supporting Information Fig. S11). The more significant source of error involves the choice of the glass transition temperature. This is fixed at 725 °C in Tucker et al. (2019) and 825 °C in Moore et al. (2015) (dashed and solid magenta line; Fig. 8a) for simplicity, but in reality, varies as a function of

764 cooling rate and melt viscosity (and, by extension, melt composition; Giordano et
 765 al., 2005; MacLennan, 2017). The average glass transition temperatures predicted by
 766 the bubble-growth python code MIMiC (which uses the model of Giordano et al.,
 767 2005; Rasmussen et al., 2020) for bubble-bearing F8 melt inclusions for cooling rates
 768 of 10 °C/s is 680 °C (dotted magenta line; Fig. 8a). Following Tucker et al. (2019),
 769 we multiply the density obtained from the pure-CO₂ EOS by the mole fraction of
 770 CO₂ (X_{CO_2}) in the vapor phase determined in VolatileCalc (Newman & Lowenstern,
 771 2002). This correction neglects the non-ideal mixing of H₂O and CO₂ at magmatic
 772 temperatures compared to the use of a mixed H₂O-CO₂ EOS (e.g., Moore et al.,
 773 2015) but is probably a reasonable approximation for relatively dry systems such as
 774 Kilauea (Fig. 5a-b).

775 The dominant control of the glass CO₂ content on the internal pressure of the
 776 inclusion in relatively anhydrous melts, and the positive relationship between the in-
 777 ternal pressure and ρ_{CO_2} from the EOS evaluated at a constant temperature, means
 778 that predicted ρ_{CO_2} values increase with increasing glass CO₂ contents (Fig. 8a).
 779 Predicted CO₂ densities from Tucker et al. (2019) plot on or below the quadratic fit
 780 through the EOS predictions for F8 melt inclusions at 725 °C (magenta solid line),
 781 because of the higher values of X_{H_2O} (and thus lower X_{CO_2}) for a number of melt
 782 inclusions which possess high glass H₂O, but low glass CO₂ contents (Fig. 5c). How-
 783 ever, unlike the predictions from the EOS method, there is no correlation between
 784 ρ_{CO_2} measured using Raman spectroscopy and glass CO₂ contents ($R^2=0.11$). In-
 785 terestingly, all melt inclusions with >200 ppm CO₂ in the glass have vapor bubbles
 786 which did not produce a FD (diamond symbols; Fig. 8a), indicating that their CO₂
 787 densities were below the detection limit of Raman Spectroscopy ($\sim 0-0.02$ g/cm³;
 788 green bar in Fig. 4c). It seems implausible that these bubbles could possess the
 789 high CO₂ densities predicted by the EOS ($\rho_{CO_2} > 0.2$ g/cm³) and fail to produce
 790 a FD. Furthermore, melt inclusions with $\rho_{CO_2} > 0.2$ g/cm³ will consist of an outer
 791 shell of liquid CO₂, and an inner sphere of vapor CO₂ at room temperature ($\sim 21-$
 792 22 °C). For $\rho_{CO_2}=0.4$ g/cm³, this liquid phase will comprise 26% of the radius of
 793 the bubble, and the motion of the inner sphere of vapor by Brownian motion would
 794 be readily observable under an optical microscope. Yet, we observe no two-phase
 795 bubbles, and there are no reports of two-phase bubbles in the Kilauean literature.

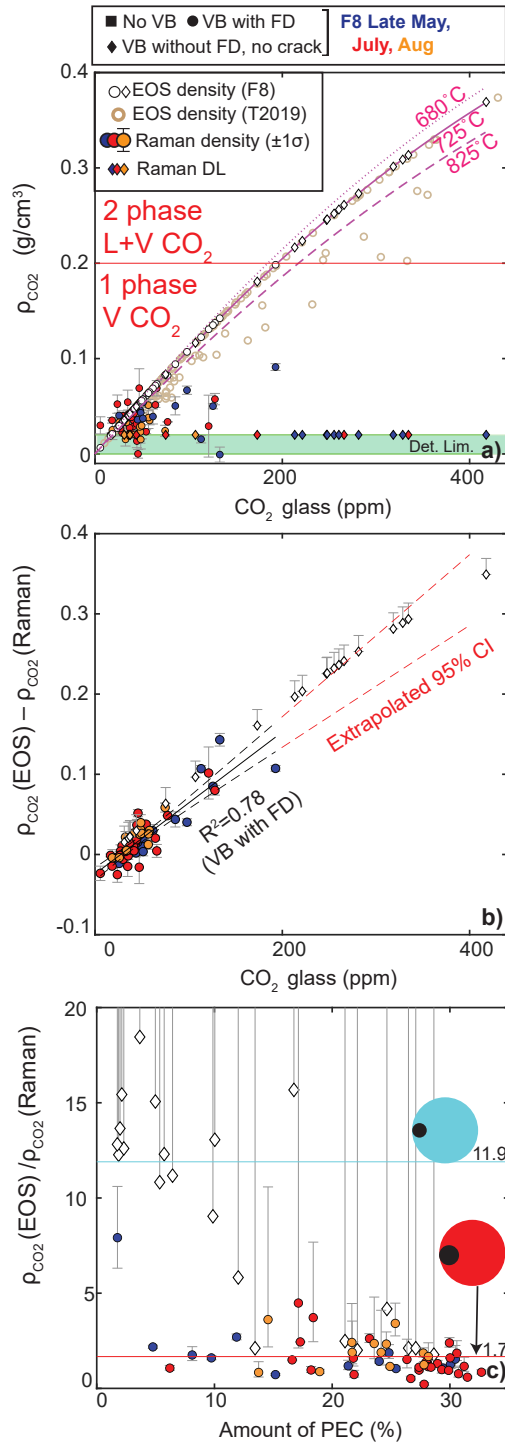


Figure 8. Comparisons of bubble CO₂ densities calculated using the EOS with those measured by Raman Spectroscopy. a) Calculated ρ_{CO_2} correlates strongly with glass CO₂. Bubbles within F8 melt inclusions are shown as white circles and diamonds (FD and no FD), bubbles within melt inclusions from Tucker et al. (2019) are shown as beige hollow circles. Magenta lines shows quadratic fits through calculated bubble densities for F8 melt inclusions for the EOS evaluated at 680°C, 725°C and 825°C. A number of inclusions with low inclusion CO₂ contents and high H₂O contents from Tucker et al. (2019) lie below this line, because of their higher X_{H_2O} values (Fig. 5c). Measured ρ_{CO_2} in this study are shown as colored circles, with error bars showing the 1σ of repeated acquisitions of each bubble. Colored diamonds (no FD, not cracked) are plotted at 0.02 g/cm³ (the presumed detection limit of Raman Spectroscopy; see Fig. 4c). b) The absolute discrepancy between predicted and measured ρ_{CO_2} , $\Delta \rho_{CO_2}$, correlates strongly with glass CO₂ content. The 95% confidence interval on a linear regression for measured bubble densities is shown with red dotted lines. Bubbles which did not produce a FD lie within error of the extrapolated confidence interval (assuming $\rho_{CO_2} = 0.02$ g/cm³). c) To allow comparison with bubble growth models in Fig. 9, the discrepancy between EOS methods and Raman measurements are shown as a factor (as above, VB without a FD assumed to contain 0.02 g/cm³). The proportion of the total bubble volume grown during quench for the High- and Low-Fo models shown in Fig. 9 are shown with red and cyan lines respectively. Error bars in b) and c) for VB with FD show the 1σ uncertainty of repeated Raman measurements, and those for VB without FD are calculated for DL between 0–0.02 g/cm⁻³ (hence they extend to infinity in c).

796 The fundamental tenet of the EOS method used by Tucker et al. (2019) is that
797 CO₂ continues to partition between the vapor bubble and the melt until the bubble
798 stops growing at the glass transition temperature. However, during syn-eruptive
799 quenching, the strong temperature dependence of CO₂ diffusivity means that the
800 diffusion of CO₂ from the melt into the bubble may cease before the bubble reaches
801 its final volume (Anderson and Brown, 1993). Continued bubble growth without
802 concurrent diffusion causes the density of CO₂ within the bubble to drop below that
803 predicted from the EOS (Aster et al., 2016; Moore et al., 2015; MacLennan, 2017).
804 Non-equilibrium bubble expansion has been proposed to account for the presence
805 of vapor bubbles in Icelandic melt inclusions with CO₂ concentrations below the
806 detection limit of Raman Spectroscopy (Neave et al., 2014).

807 The discrepancy between EOS predictions and Raman measurements ($\Delta \rho_{CO_2}$)
808 increases linearly with glass CO₂ content ($R^2=0.75$; shown as an absolute discrep-
809 ancy, Fig. 8b) and decreases with the amount of PEC (shown as a factor, Fig. 8c).
810 Melt inclusions containing bubbles without a FD lie within the confidence interval
811 of the regression through bubbles which produced a FD if the Raman detection
812 limit (0.02 g/cm³) is subtracted from CO₂ densities calculated from the EOS (Fig.
813 8b). To investigate these correlations, we assess the relative contribution of bubble
814 growth at high magmatic temperatures during PEC and ascent (where CO₂ diffusion
815 and bubble growth are coupled) compared to bubble growth during quench (where
816 CO₂ diffusion is temperature-limited, and therefore decoupled from the mechanical
817 expansion of the bubble).

818 We model melt inclusions from the point of entrapment to the glass transition
819 temperature using the model of MacLennan (2017; Fig. 9). Quench rates of 10°C/s
820 were used based on video footage of the sampling and quenching of the Aug-18 sam-
821 ple; ~40 s elapsed between the sample being pulled from the channel (~1150°C)
822 and becoming brittle at the glass transition temperature (~725 °C Tucker et al.,
823 2019). At these cooling rates, there is negligible transfer of CO₂ from the melt to
824 the bubble during syn-eruptive quenching. Two end-member cooling histories were
825 modelled. The red melt inclusion in Figure 9a experienced large amounts of cooling
826 ($\Delta T=150^\circ\text{C}$) and PEC at high magmatic temperatures and pressures, representa-
827 tive of the PT path followed by melt inclusions hosted within the most forsteritic
828 olivines. The blue melt inclusion in Figure 9b experiences no cooling and post-

829 entrapment crystallization prior to ascent and syn-eruptive quenching, representative
 830 of Low-Fo melt inclusions which form in carrier melts with similar temperatures to
 831 the melts in which they were erupted.

832 The High-Fo melt inclusion (red) grows a considerable proportion of its final
 833 bubble volume (58%) during PEC at high magmatic temperatures (square to star
 834 symbol; Fig. 9a). The diffusion of CO₂ into this growing bubble causes the CO₂
 835 content of the melt phase to drop rapidly (Fig. 9c). During syn-eruptive quenching,
 836 there is no further CO₂ diffusion between the melt and bubble (Fig. 9c). This stage
 837 of bubble growth accounts for 42% of the final volume, with ρ_{CO_2} decreasing from
 838 0.10 to 0.06 g/cm³ (Fig. 9a, d). As the EOS method effectively predicts the density
 839 of CO₂ in the vapor bubble prior to the final, quench-induced stage of bubble ex-
 840 pansion, the EOS method overpredicts the CO₂ density by a factor of 1.7× in this
 841 example. This lies well within the deviation between measured and predicted CO₂
 842 contents for High-Fo F8 melt inclusions which have experienced >10% PEC (red
 843 line on Fig. 8c). In reality, the proportion of the bubble grown at high temperatures
 844 will be substantially greater, as the model of Maclennan (2017) does not account for
 845 the FeO-loss process, which greatly increases the amount of PEC for a given ΔT .
 846 The volume of the bubble grown during syn-eruptive quench is determined by the
 847 difference between the temperature at the initiation of syn-eruptive quenching, and
 848 the glass transition temperature, so is almost constant for different PT paths. In
 849 contrast, with increasing amounts of PEC, the volume of the bubble grown at high
 850 temperatures gets progressively larger, so the relative expansion of the bubble during
 851 quench (and therefore the change in CO₂ density) gets progressively smaller. For
 852 example, in models with $\Delta T=200^\circ\text{C}$ instead of $\Delta T=150^\circ\text{C}$, the amount of PEC
 853 increases from 18% to 25%, and the volume proportion of the bubble grown at high
 854 temperature increases from 58% to 68%. In turn the bubble density drops from only
 855 0.073 to 0.052 g/cm³ during syn-eruptive quenching (so the EOS method would only
 856 over predict by a factor of $\sim 1.4\times$).

857 In contrast, the Low-Fo melt inclusion (blue) grows a very small proportion of
 858 its total bubble volume at high temperatures (10%), with 90% of the final bubble
 859 volume growing upon quench (Fig. 9b). Substantial bubble expansion upon quench
 860 without concurrent CO₂ diffusion causes ρ_{CO_2} to drop substantially (Fig. 9d). Ef-
 861 fectively, the EOS method calculates the density of the bubble at the initiation of

862 the quench stage ($\rho_{CO_2}=0.205$ g/cm³; star symbol), while the true bubble density
863 is $11.9\times$ lower ($\rho_{CO_2}=0.021$ g/cm³; circle symbol), close to the detection limit of
864 Raman spectroscopy. This calculated discrepancy is very similar to that for vapor
865 bubbles in Low-Fo inclusions which do not have Fermi diads (assuming the detection
866 limit= 0.02 g/cm³, cyan line, Fig. 8c).

867 In summary, the EOS substantially overestimates ρ_{CO_2} for melt inclusions
868 which have experienced small amounts of PEC and retain high CO₂ contents (Fig.
869 8b,c), because bubble growth in these melt inclusions is dominated by the quench-
870 ing process where there is no diffusion of CO₂ into the bubble. In contrast to these
871 very large discrepancies (factors of ~ 10), bubble densities in melt inclusions which
872 have experienced extensive PEC are broadly matched by the EOS method (within a
873 factor of ~ 2 ; Fig. 8c).

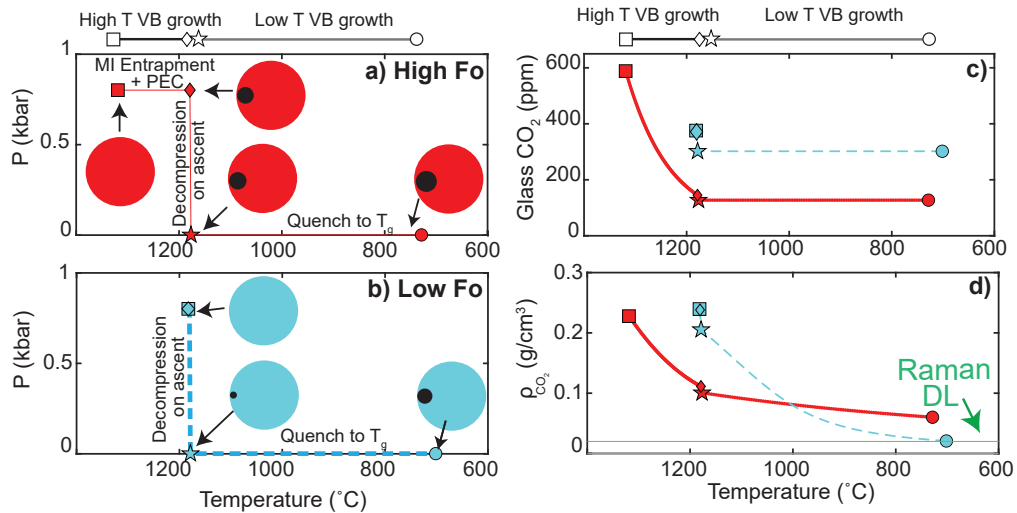


Figure 9. Model of CO₂ partitioning between the melt and bubble for PT scenarios representative of inclusions hosted within High and Low-Fo olivines (red and blue colors, respectively). a) The red melt inclusion experiences considerable cooling ($\Delta T=150^\circ\text{C}$) and post-entrapment crystallization at high temperatures and pressures (square to diamond symbol), driving the growth of a vapor bubble. This high temperature phase of bubble growth is accompanied by CO₂ diffusion from the melt to the bubble, causing the glass CO₂ content to drop substantially (c). This inclusion then ascends to the surface (diamond to star symbol), and experiences a second stage of vapor bubble growth during syn-eruptive quenching (star to circle symbol). b) The blue melt inclusion follows an end-member PT path representative of an inclusion hosted within a Low-Fo olivine. It experiences no cooling and post-entrapment crystallization at high temperature. A bubble only begins to grow during ascent to the surface, with 90% of the total bubble volume of this inclusion occurs during syn-eruptive quenching (star to circle). At the quenching rates of 10°C/s used in this model, there is negligible CO₂ transfer from the glass to the bubble during this low temperature phase of bubble growth. The large amount of bubble expansion without concurrent CO₂ diffusion causes the density of CO₂ in the vapor bubble to drop close to the detection limit of Raman Spectroscopy (green line, d), while the CO₂ of the glass phase remains unchanged (c).

874 These bubble-growth models show that the magnitude of the discrepancy be-
 875 tween measured bubble densities and those predicted by the EOS relates to the
 876 proportion of the bubble grown during syn-eruptive quenching. In contrast, Tucker
 877 et al. (2019) suggest that Raman measurements may underestimate ρ_{CO_2} relative to

EOS methods because of the sequestration of significant quantities of CO₂ as thin
films of solid carbonate on bubble walls. Carbonate phases have been identified in a
number of melt inclusion vapor bubbles from subduction zone settings based on the
presence of a distinctive peak in the Raman spectra at $\sim 1090\text{ cm}^{-1}$ (Venugopal et
al., 2020; Moore et al., 2015). However, while Moore et al. (2015) report relatively
abundant carbonate phases in vapor bubbles from Seguam and Fuego, only four of
the 142 Kilauean vapor bubbles they examined contained carbonates, all of which
were hosted within a single olivine crystal. This suggests that vapor bubble carbon-
ates are significantly less common in H₂O-poor ocean island systems. We observe no
carbonate peaks in Raman spectra from F8 bubbles, nor during optical observations
made prior to the exposure of bubbles during polishing. Additionally, no carbonate
phases were identified during detailed examination of exposed bubble walls using
backscatter and secondary electron imaging, and Energy-Dispersive Spectroscopy
(EDS) maps on a FEG-SEM. These EDS maps reveal that bubble wall coatings with
a “dotted” appearance identified by Tucker et al. (2019) (see their Fig. 2F) consist
of Fe-Cu sulfides, rather than carbonates (see also Venugopal et al., 2020; Moore et
al., 2015; Wieser, Jenner, et al., 2020). Finally, even if carbonates in bubble walls
remained undetected, our observations regarding the systematic relationship between
PEC amounts, CO₂ contents, and the discrepancy between Raman measurements
and the EOS would necessitate that only bubbles hosted in melt inclusions which
had undergone negligible PEC contain carbonate phases.

5.5 Reconstructing Magma Storage Depths

Under the assumption that any reservoir from which a substantial proportion
of the crystal cargo was derived must also have supplied melt (in order to entrain
these crystals, and carry them to the surface), the depths of the main magma reser-
voirs supplying F8 can be estimated from melt inclusion entrapment pressures (for a
known crustal density). Entrapment pressures were calculated from PEC-corrected
total CO₂ and major element contents, and temperatures calculated using the MgO-
liquid thermometer of Helz and Thornber (1987) for PEC-corrected MgO contents.
As melt inclusion H₂O contents have been reset by diffusive re-equilibration, satu-
ration pressures were calculated assuming H₂O=0.5 wt%, based on the distribution
of measured H₂O contents in literature studies of Kilauean melt inclusions and un-

910 degassed submarine glasses from the ERZ (Fig. 5b; Sides, Edmonds, Maclennan,
 911 Houghton, et al., 2014; Sides, Edmonds, Maclennan, Swanson, & Houghton, 2014;
 912 Clague et al., 1995; Dixon et al., 1991; Tucker et al., 2019). Entrapment pressures
 913 for measured water contents are also shown in the Supplementary Information. En-
 914 trapment pressures were converted into magma storage depths assuming $\rho=2400$
 915 kg/m^{-3} (for consistency with modelling of the geodetic signals from the 2018 sum-
 916 mit collapse by Anderson et al., 2019). Initially, we consider melt inclusions with no
 917 vapor bubble, or a vapor bubble which produced a FD, due to the uncertainty in the
 918 CO_2 density of vapor bubbles which do not contain a FD.

919 Literature studies of Kīlauean melt inclusions have mostly calculated satura-
 920 tion pressures using the $\text{CO}_2\text{-H}_2\text{O}$ solubility model of Dixon et al. (1995) and Dixon
 921 (1997), implemented in the excel workbook VolatileCalc (Newman & Lowenstern,
 922 2002, e.g., Tuohy et al. 2016; Sides et al. 2014a, b; Moore et al., 2015; Tucker et al.,
 923 2019). VolatileCalc-Basalt uses a simplified relationship for the compositional de-
 924 pendence of CO_2 solubility expressed in terms of just the melt SiO_2 content, rather
 925 than the full compositional parameter Π which accounts for the abundance of seven
 926 cations (Dixon, 1997, Fig. 6c). In this simplification the parameter $X_{\text{CO}_3^{2-}}(P_0, T_0)$,
 927 which represents the mole fraction of the carbonate ion in equilibrium with a spec-
 928 ified fluid CO_2 fugacity at 1200 °C and 1 bar in the thermodynamic expression of
 929 Dixon et al. (1995), is expressed as:

$$X_{\text{CO}_3^{2-}}(P_0, T_0) = 8.7 \times 10^{-6} - 1.7 \times 10^{-7}[\text{SiO}_2] \quad (6)$$

930 This relationship derives from the excellent linear correlation between Π and
 931 SiO_2 in a suite of lavas with 40–49 wt% from the North Arch Volcanic field (blue
 932 regression line; Fig. 6c; Dixon et al., 1997). However, extrapolation of Equation 6
 933 beyond 51.2 wt% SiO_2 returns a negative value for $X_{\text{CO}_3^{2-}}(P_0, T_0)$, which, in turn,
 934 predicts that the solubility of CO_2 is negative at all pressures. To avoid these ex-
 935 trapolation issues, VolatileCalc-Basalt does not let users enter a SiO_2 content >49
 936 wt%, so most studies simply calculate the CO_2 solubility for melts with >49 wt%
 937 SiO_2 using the expression for $\text{SiO}_2=49$ wt% (e.g., Tucker et al., 2019; Sides, Ed-
 938 monds, Maclennan, Houghton, et al., 2014; Sides, Edmonds, Maclennan, Swanson,
 939 & Houghton, 2014). Newman and Lowenstern (2002) suggest that this approxima-

940 tion should return accurate entrapment pressures for basaltic compositions with up
941 to 52 wt% SiO₂ contents. However, the simplified compositional parameter used in
942 VolatileCalc-Basalt is only valid for melt compositions which define the same tra-
943 jectories in Π vs. SiO₂ space as the North Arch Lavas. F8 melt inclusions which
944 have undergone >10% PEC are offset to substantially higher Π values at a given
945 SiO₂ (Fig. 6c), so VolatileCalc-Basalt underestimates the solubility of CO₂. Addi-
946 tionally, while F8 melt inclusions show a large drop in Π with increasing SiO₂, all
947 but four melt inclusions have SiO₂ >49 wt%, so are treated as if they had the same
948 composition in VolatileCalc-Basalt (red line; Fig. 6c). Thus, VolatileCalc-Basalt not
949 only underestimates CO₂ solubility, and therefore overestimates entrapment pres-
950 sures for F8 melt inclusions hosted in High-Fo olivines, it also neglects compositional
951 variations in CO₂ solubility within this suite (Fig. 6c).

952 To demonstrate the importance of evaluating the suitability of different solu-
953 bility models, we compare entrapment pressures from VolatileCalc-Basalt with the
954 models of Ghiorso and Gualda (2015), hereafter MagmaSat, Iacono-Marziano et
955 al. (2012) with hydrous coefficients, hereafter IM-2012, and Shishkina et al. (2014),
956 hereafter S-2014, using the open-source python tool VESIcal (Iacovino et al., 2020).
957 These three models utilize more than a decade of additional experiments on basaltic
958 compositions compared to the expressions implemented in VolatileCalc-Basalt. By
959 extension, these models are calibrated on a significantly larger compositional range
960 (Fig. 6a), so more effectively encapsulate variability in CO₂ solubility as a function
961 of melt composition.

962 Entrapment pressures for melt inclusions hosted in Low-Fo olivines from F8
963 calculated using VolatileCalc-Basalt, S-2014, and IM-2012 are statistically indistin-
964 guishable using the KS test at $p=0.05$ (Fig. 10a), likely because the major element
965 compositions of these melt inclusions lie within the calibration range of all four sol-
966 ubility models (Fig. 6a). MagmaSat returns slightly lower pressures, although these
967 are not statistically distinguishable ($p=0.1$ vs. S-2014). These slight discrepancies
968 likely reflect the differential treatment of mixing between H₂O and CO₂ fluids in
969 these different models (e.g., non-ideal mixing in MagmaSat and IM-2012 vs. ideal
970 mixing in S-2014 and VolatileCalc-Basalt; see Supporting Information Fig. S1).
971 As only 2 Low-Fo melt inclusions have vapor bubbles producing a FD ($N=2$), the
972 distribution of entrapment pressures calculated using just glass CO₂ contents are

973 indistinguishable from those using total CO₂ contents (dotted magenta vs. solid red
974 lines; Fig. 10a).

975 In contrast, there are substantial differences between the entrapment pressures
976 obtained from different solubility models for High-Fo melt inclusions ($>F_{O_{81.5}}$), with
977 MagmaSat and S-2014 plotting to significantly lower pressures than IM-2012 and
978 VolatileCalc-Basalt (both pairs are statistically indistinguishable from one another
979 at $p=0.05$; Fig. 10b). As discussed above, the simplification of the compositional
980 dependence in VolatileCalc-Basalt means that this model underestimates CO₂ solu-
981 bility, and therefore overestimates entrapment pressures for High-Fo melt inclusions
982 (Fig. 6c). Similarly, Iacono-Marziano et al. (2012) warn that their semi-empirical
983 model poorly incorporates the compositional effect of melt MgO contents on CO₂
984 solubility, as the vast majority of melts in their calibration dataset have $\sim 6\text{--}8$ wt%
985 MgO. In contrast, High-Fo PEC-corrected melt inclusions have MgO contents rang-
986 ing from 7.8–13.7 wt% (Fig. 6a). The calibration dataset for the S-2014 model
987 incorporates a significantly broader range of basaltic compositions, including melts
988 with MgO contents similar to PEC-corrected High-Fo melt inclusions (Fig. 6a). The
989 MagmaSat calibration dataset is similarly extensive (including the experiments used
990 to calibrate S-2014, IM-2012 and VolatileCalcBasalt). As for Low-Fo melt inclusions,
991 MagmaSat is offset to slightly lower pressures than S-2014 (median offset of 0.1
992 kbar).

993 Overall, we favour entrapment pressures from MagmaSat (Fig. 11, as it has
994 the largest calibration dataset, and is a full thermodynamic model (whereas S-2014
995 is purely empirical). Additionally, the S-2014 model is parameterized such that it
996 predicts that ~ 1 wt% H₂O dissolves at 0 bar, meaning that saturation pressure
997 calculations are effectively evaluating the solubility of pure CO₂ for the H₂O con-
998 tents considered here (so saturation pressure does not change for H₂O contents
999 between 0–1 wt% H₂O, see Supporting Information Fig. S1). As shown in Fig. 10,
1000 differences between Shishkina and MagmaSat are relatively small. For High-Fo inclu-
1001 sions, the differences between these models are statistically insignificant, and easily
1002 overwhelmed with the errors associated with bubble volumes (error bars on Fig.
1003 11a). For completeness, Supporting Information Fig. S12 shows forsterite vs. depth
1004 plots similar to those shown in Fig. 11 for reconstructions using Shishkina, and for
1005 measured and fixed H₂O contents.

1006 Using MagmaSat, Low-Fo melt inclusions yield median entrapment depths
1007 (assuming $\rho=2400 \text{ kg/m}^{-3}$) of 1.44 km (lower and upper 68%=0.89–1.74 km). The
1008 median centroid depth, aspect ratio and reservoir volume derived from modelling of
1009 the first stage of the 2018 caldera collapse by Anderson et al. (2019) suggests that
1010 the HMM reservoir spans depths of 0.82–3.1 km. This depth range aligns well with
1011 our entrapment depths, which mainly cluster in the top half of that range (perhaps
1012 suggesting melt inclusion formation was favoured in the upper half of the reservoir).
1013 The low PEC amounts experienced by these melt inclusions, the absence of cracks,
1014 and the fact that the two Low-Fo inclusions which did yield a diad had very low
1015 CO_2 densities (Fig. 4c), suggests that melt inclusions with a vapor bubble which did
1016 not produce a FD likely contained very small quantities of CO_2 (because the bubble
1017 predominantly forming during syn-eruptive quench; Fig. 9). Thus, we also consider
1018 entrapment depths from these melt inclusions (diamond shapes on Fig. 11a). This
1019 extends the distribution of entrapment depths to slightly deeper depths, which show
1020 an even better overlap with the depths of the HMM reservoir suggested by Anderson
1021 et al. (2019).

1022 Considering only High-Fo melt inclusions with a measurable Fermi diad (due to
1023 the uncertainty in the amount of CO_2 held within vapor bubbles which did not pro-
1024 duce a FD in melt inclusions which have undergone extensive PEC), the distribution
1025 of entrapment depths (KS test, $p=1.6 \times 10^{-7}$) and means (ANOVA, $p=2.5 \times 10^{-6}$) are
1026 offset to significantly higher pressures than Low-Fo melt inclusions (Fig. 11a). Con-
1027 sidering the error associated with reconstructing bubble CO_2 contents from bubble
1028 volumes estimated from 2D images (shown in pink on Fig. 10b), the distribution of
1029 entrapment depths for High-Fo olivines overlaps remarkably well with geophysical
1030 estimates of the depth of the SC reservoir (3–5 km; Poland et al., 2015). In detail,
1031 entrapment depths for High-Fo olivines seem to form two main groups, one at ~ 2
1032 km depth, and a second at 3–5 km depth (Fig. 11a).

1033 The quench-dominated mechanism of bubble growth in Low-Fo olivines means
1034 that very little CO_2 is held within the vapor bubble. Thus, entrapment depths
1035 calculated using glass-only measurements are statistically indistinguishable from
1036 those combining bubble and glass measurements (Fig. 10a). In contrast, entrapment
1037 depths calculated using just glass CO_2 contents in High-Fo olivines are anomalously
1038 shallow (median=0.38 km, lower and upper 68%=0.3–0.51 km; Fig. 11b), because

1039 bubble growth at high temperatures during PEC has resulted in the vast majority of
1040 the CO₂ entering the vapor bubble (Fig. 9).

1041 Use of EOS techniques to reconstruct CO₂ contents of vapor bubbles yields
1042 very high entrapment depths for Low-Fo olivines (median=3.3 km, lower and up-
1043 per 68%=0.89–10.8 km; Fig. 11c). Crucially, 13 inclusions yield entrapment depths
1044 >5 km (the inferred base of the SC reservoir), because the EOS method drastically
1045 overestimates bubble CO₂ densities in inclusions which have experienced minimal
1046 PEC (Fig. 8b-c). For High-Fo olivines, there is a better overlap between entrapment
1047 depths calculated using EOS methods, and Raman measurements, and EOS meth-
1048 ods get closer to the true distribution of entrapment pressures than measurements
1049 of only the glass phase (Fig. 10b vs. c). However, EOS methods still predict that 23
1050 melt inclusions crystallized at >5 km depth, with one forming at 26.4 km, compared
1051 to only two entrapment depths at 6.3 and 8.8 km using Raman reconstructions of
1052 bubble CO₂.

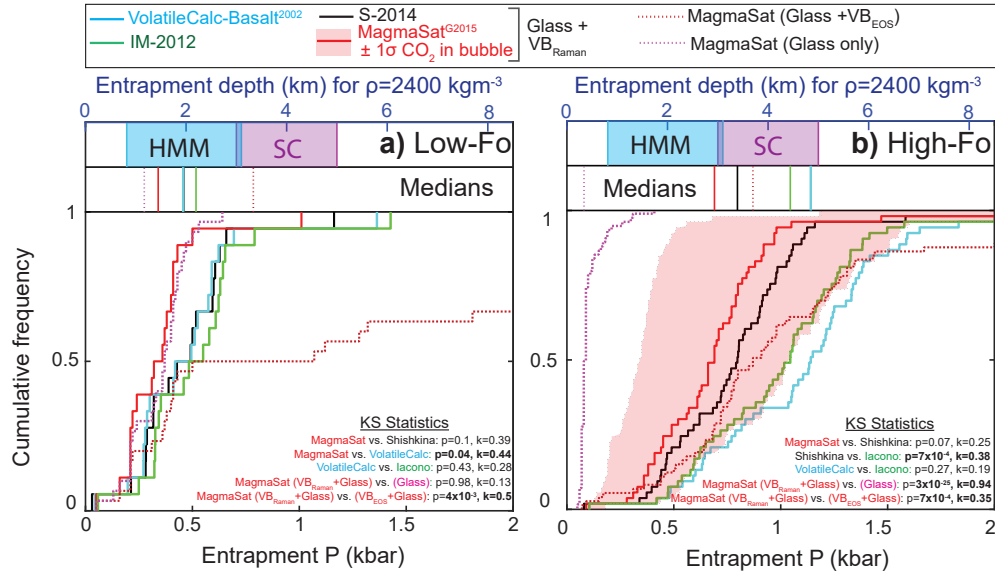


Figure 10. Cumulative distribution functions of entrapment pressures from different solubility models (major elements and CO₂ abundances corrected for the effects of PEC), with p values and test statistics from the KS test shown for different comparisons. a) Entrapment pressures for melt inclusion hosted in Low-Fo olivines (for melt inclusions with no VB, or a VB with a FD). Assuming $\rho=2400 \text{ kg/m}^3$, the median depths for all solubility models align well with the depth range of the HMM reservoir from modelling of the first stage of the 2018 caldera collapse by Anderson et al. (2019) (upper and lower limits calculated from their median volume, centroid depth, and aspect ratio; cyan bar). The distributions of entrapment pressures from MagmaSat calculated from total carbon contents (bubbles+glass; red line) vs. glass only measurements (pink dotted line) are statistically indistinguishable. Entrapment pressures from MagmaSat where bubble CO₂ contents are calculated using the EOS method lie to significantly higher pressures (deep red dotted line). b) Entrapment pressures calculated for melt inclusions hosted in High-Fo olivines (for melt inclusions with a VB producing a FD). The light red region shows the error on MagmaSat entrapment pressures resulting from uncertainty in estimating bubble proportions from 2D images (Tucker et al., 2019). Entrapment depths considering this error window align well with geophysical estimates of the depth of the SC reservoir (3–5 km, magenta bar; Poland et al., 2015). Entrapment pressures from MagmaSat calculated using only glass CO₂ contents (dotted magenta line) are offset to very low pressures. Entrapment pressures calculated from bubble reconstructed using the EOS method are offset to anomalously high pressures. In a-b), all melt inclusions are shown for glass-only measurements and EOS calculations, because studies which do not perform Raman measurements cannot distinguish between bubbles with and without a FD.

5.6 Summit-Rift Connectivity

Melt inclusion entrapment depths indicate that olivine crystals erupted at F8 crystallized within both the shallower HMM reservoir (Low-Fo olivines) and the deeper, SC reservoir (High-Fo olivines, see also Lerner, 2020). The low degrees of olivine-melt disequilibrium and limited amounts of PEC experienced by melt inclusions hosted within Low-Fo olivines implies that these crystals grew in a melt with a similar Mg#, and therefore temperature, to the carrier melt in which they were erupted. In contrast, the high degrees of olivine-melt disequilibrium and large amounts of PEC indicates that High-Fo crystals were mixed into a significantly lower Mg# (and therefore cooler) carrier liquid than the liquid in which they crystallized. Based on reports of lattice distortions (Gansecki et al., 2019) in some F8 olivines, high core forsterite contents, and the clustering of entrapment pressures between 3–5 km (Fig. 11), we suggest that these olivines grew in the SC reservoir, and then settled into mush piles at the base of this reservoir where they were stored for prolonged periods (perhaps as long as centuries to millenia; Wieser, Edmonds, et al., 2020).

Seismic swarms and the initiation of inflationary tilt in March to April 2018 have been interpreted to record the injection of new melts into the South Caldera reservoir (Neal et al., 2019; Flinders et al., 2020), which may have disturbed the olivine mush pile. These new melts (along with the High-Fo olivines they scavenged) would then have mixed into the cooler, lower Mg# melts present within the middle to upper parts of the SC reservoir. Alternatively, if inflationary signals were generated by a reduction in the amount of magma flowing along the ERZ to Pu‘u ‘Ō‘ō (Patrick et al., 2020), progressive internal pressurization of the SC reservoir could also disturb piles of settled crystals. Rapid cooling of mush-derived olivines following their mixing into more evolved melts would have initiated large amounts of PEC. Using the method of Danyushevsky et al. (2002, 2000), the degrees of Mg# re-equilibration between melt inclusions and host olivine crystals (~70-100%) indicate that crystals were resident in these cooler melts for timescales of approximately a month to a year prior to their eruption at Fissure 8. This is consistent with the time lag between geophysical signals indicating increasing pressurization of the magmatic system in March, and the eruption of crystals between late May and August.

1085 The fact that only two melt inclusions record entrapment depths >5 km rules
1086 out models where high forsterite olivines grew in deeper magma storage reservoirs
1087 near the base of the volcanic pile (as suggested for Kīlauea’s prehistoric explosive
1088 period by Lynn et al., 2017), or within Kīlauea’s deep rift zones at ~ 6 – 9 km (Fig 11
1089 Clague & Denlinger, 1994).

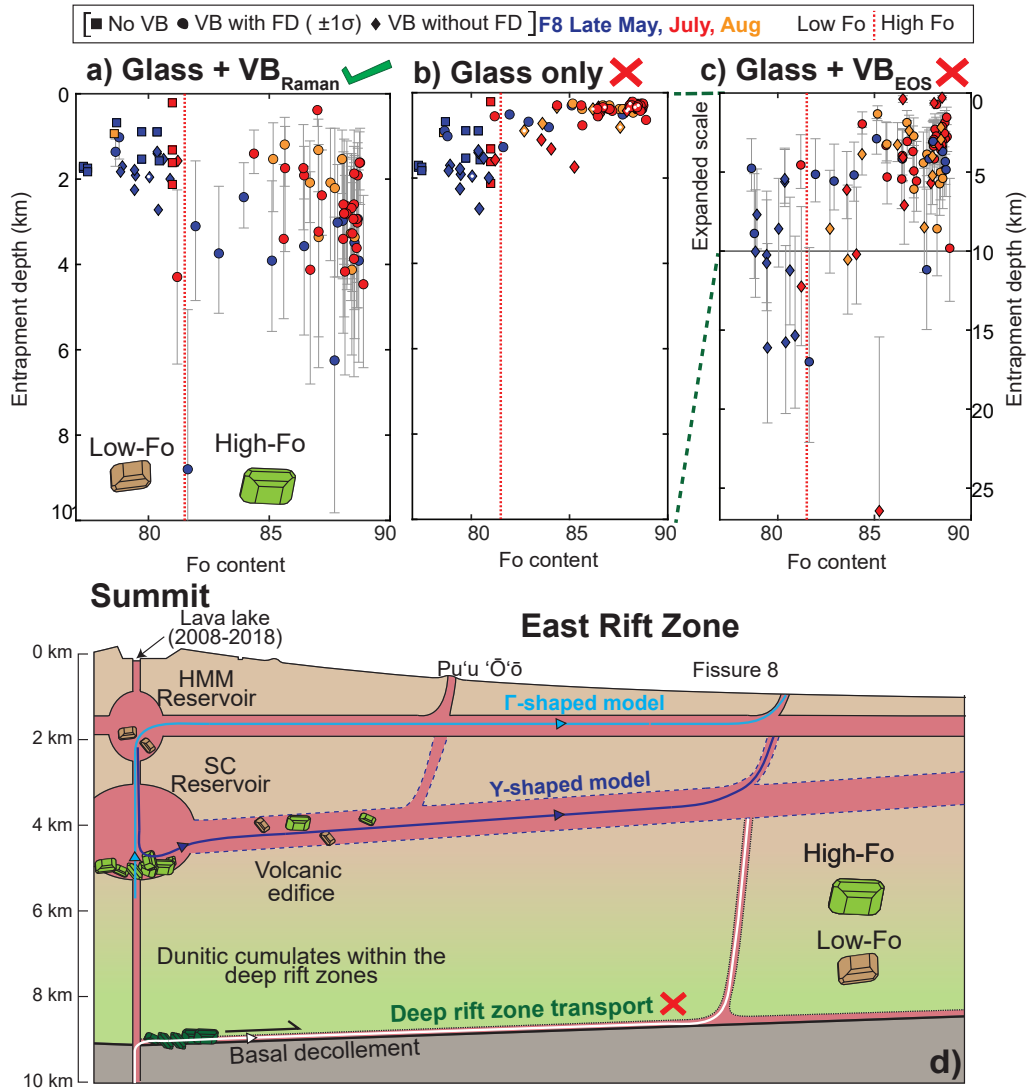


Figure 11.

1090 **Caption Fig. 11.** Schematic diagram of Kilauea's plumbing system, informed
 1091 by entrapment depths from MagmaSat for PEC-corrected melt inclusion compo-
 1092 sitions (assuming $\rho=2400 \text{ kg/m}^3$ following Anderson et al. (2019)). a) Preferred
 1093 entrapment depths from this study (all melt inclusions for Low-Fo olivines, only
 1094 those with a FD for High-Fo olivines). Error bars on bubble-free melt inclusions
 1095 from SIMS analyses are smaller than the symbol size. Error bars for bubble-bearing
 1096 melt inclusions were calculated from the minimum and maximum possible total CO_2
 1097 content using the 1σ error calculated from repeated Raman analyses of each bubble,
 1098 and the 1σ estimated by Tucker et al. (2019) associated with calculating 3D bubble

1099 volume proportions from 2D images (-48 to 37%). b) Entrapment depths estimated
1100 from analyses of only the glass phase are anomalously shallow for High-Fo olivines.
1101 c) Entrapment depths using the EOS method to reconstruct bubble CO₂ contents
1102 are anomalously deep, with large numbers of inclusions plotting at >5 km depth
1103 (note change in scale). Error bar reflects the uncertainty associated with calculat-
1104 ing 3D bubble volume proportions from 2D images. d) Cross section showing the
1105 three hypothesized magma transport paths supplying rift zone eruptions. Depths are
1106 defined as the vertical distance beneath Kīlauea’s summit.

1107 The mechanism by which crystal populations grown in the HMM and SC
1108 reservoirs were mixed into a single carrier melt encapsulates an ongoing debate at
1109 Kīlauea regarding the geometry of the connection between the rift zone conduit and
1110 the summit reservoir system. This connection has been variably described as a Y-
1111 shaped feeder system with the SC reservoir feeding both the HMM reservoir and the
1112 ERZ with two discrete conduits (Pietruszka et al., 2018; Poland et al., 2015, Model
1113 2, Fig. 11d), or a Γ -shaped feeder system with a vertical conduit between the HMM
1114 and the SC reservoir, and a single, near-horizontal conduit from the HMM reservoir
1115 into the ERZ (Cervelli & Miklius, 2003, Model 3, Fig. 11d). Cervelli and Miklius
1116 (2003) suggest that the Γ -shaped model is more plausible because a shallow conduit
1117 (which is subject to less lithostatic pressure) is more likely to remain open during
1118 pauses in eruptive activity than a deep conduit, and because shallow intrusions
1119 into the upper ERZ influence both the HMM reservoir and activity at Pu‘u Ō‘ō.
1120 However, Poland et al. (2015) favour the Y-shaped model based on earthquake and
1121 InSAR observations that dyke intrusions into the ERZ in 2007 and 2011 ascended
1122 from a depth of \sim 2–3 km.

1123 For both reservoir geometries, the olivine mush pile at the base of the SC
1124 reservoir may have been disturbed by the input of new magma into Kīlauea’s sum-
1125 mit inferred from geophysical signals (Neal et al., 2019; Flinders et al., 2020), or
1126 progressive internal pressurization due to a drop in magma output to Pu‘u Ō‘ō.
1127 In the Γ -shaped model, High-Fo crystals sourced from the SC mush pile may have
1128 ascended into the HMM reservoir, and then been transported along a shallow rift
1129 zone conduit to the site of the eruption along with Low-Fo olivines. However, the
1130 Y-shaped model provides an additional mechanism by which to disturb the SC mush
1131 pile. In this geometry, melts from the HMM reservoir carrying Low-Fo olivine crys-

1132 tals would have drained down through the SC reservoir before passing out onto
1133 the rift zone, with significant potential for this downward flow, aided by the large
1134 scale collapse of Kīlauea’s caldera, to erode the SC mush pile. Interestingly, the pro-
1135 portion of crystals which are out of equilibrium with their carrier melts increases
1136 substantially between May-August 2018 (Fig. 2a), and the degree of re-equilibration
1137 between melt inclusions and host crystals decreases (Fig. 3b).

1138 If the disturbance to the mush pile was solely the result of pressurization of
1139 the volcanic plumbing system, it might be expected that the majority of High-Fo
1140 olivines were disturbed from their mush piles in mid-March to April 2019, when in-
1141 flationary signals were the strongest (Patrick et al., 2020; Neal et al., 2019). In this
1142 scenario, High-Fo olivines might be expected to be more dominant in the May-18 vs.
1143 July and Aug-18 samples. In contrast, increasing erosion and scavenging of High-
1144 Fo olivines during the downdraining of melts from the HMM reservoir into the SC
1145 reservoir during the summit collapse could account for the increase in the proportion
1146 of High-Fo olivines with time, similar to the mechanism suggested by Teasdale et al.
1147 (2005) for the 1998 eruption of Cerro Azul, Galápagos. Erosion of the mush pile by
1148 down-draining from the shallower HMM reservoir, into which the summit caldera
1149 was collapsing, also accounts for the fact that High-Fo olivines were extremely rare
1150 during the 35 year Pu‘u ‘Ō‘ō eruption.

1151 Another possibility is that some melt inclusions were trapped during the 40
1152 km of transport down the ERZ to the site of the eruption (Patrick et al., 2019).
1153 Assessment of this hypothesis requires assumptions regarding the depth of magma
1154 transport. Given that the dyke to the LERZ propagated downrift from Pu‘u ‘Ō‘ō,
1155 we assume that the dyke had a similar depth to intrusions within the proximity of
1156 Pu‘u ‘Ō‘ō between 1997–2007, which have been studied in detail, and shown to rise
1157 from the ERZ conduit at depths of ~ 2 –2.4 km (Owen et al., 2000; Montgomery-
1158 Brown et al., 2011, and refs within). Thus, it is plausible that some of the Low-Fo
1159 olivines with entrapment depths near ~ 2 km may have growth in the rift zone. How-
1160 ever, crystallization within the ERZ conduit and dyke would likely occur throughout
1161 the eruption, yet the abundance of Low-Fo olivine crystals declines as the eruption
1162 proceeds

1163 The cluster of High-Fo olivines at ~ 2 km could also represent crystallization
1164 during down-rift transport. These olivine crystals have Fo contents between 84 and
1165 89, which must have grown from melts with MgO contents between 8.5–13.1 wt%
1166 (for $K_D=0.3$, $\text{FeO}_T=11.33$ wt%, with $\text{Fe}^{3+}/\text{Fe}_T=0.15$). Yet, the highest erupted
1167 glass MgO content during the 2018 LERZ eruption is 6.74 wt% MgO (Fig. 3a and
1168 Gansecki et al., 2019). Moreover, glass MgO contents during the 35-year Pu‘u ‘Ō‘ō
1169 eruption did not exceed 8 wt% MgO (see Fig. 8.2 Thornber et al., 2015), suggesting
1170 that high MgO melts may not have been present in the rift zone conduit since the
1171 early phases of the Mauna Ulu eruption in 1969 (Wieser et al., 2019). In contrast,
1172 based on the occurrence of high MgO glass shards in a number of eruptions around
1173 the summit caldera, Helz et al. (2015) suggest that melts with 6.5–11 wt% MgO are
1174 present in the summit reservoir over many centuries. This supports our inference
1175 that the High-Fo olivines erupted at F8 crystallized from high MgO melts supplied
1176 from the Hawaiian mantle plume within the SC reservoir. These high MgO melts are
1177 very rarely erupted at the surface as they rapidly mix with more evolved, resident
1178 melts within the reservoir, so the only record of their existence are the olivines they
1179 crystallize. Given the rarity of these high MgO melts at the surface, it is difficult to
1180 imagine a situation where these melts would avoid mixing with resident magmas in
1181 the summit reservoir, and manage to travel prolonged distances along the ERZ con-
1182 duct (which must be dominated by low MgO melts based on the composition of the
1183 co-erupted carrier liquid at F8). Finally, if these High-Fo olivines crystallized in the
1184 rift zone, they must have been resident for between a month and a year before they
1185 erupted at F8 (based on the degree of Mg# re-equilibration between melt inclusions
1186 and host olivine crystals).

1187 Interestingly, the May-18 sample does not show the distinctive clustering of
1188 High-Fo entrapment depths at ~ 2 km seen in the July and Aug-18 sample. This
1189 may result from the relatively small number of measurements of High-Fo olivines in
1190 this sample ($N=12$). Alternatively, it may suggest that the two reservoirs became
1191 increasingly connected during the collapse of the summit caldera, allowing remobi-
1192 lized High-Fo crystals from the SC mush pile to be transported up into the shallower
1193 HMM reservoir. The juxtaposition of these hot crystals with cooler melts within this
1194 reservoir may have led to dissolution or rapid growth (Shea et al., 2019; Mourey et
1195 al., 2020), favouring the formation of embayments. Perhaps due to the mixing with

1196 a hotter, and higher Mg# melt, growth may have resumed, sealing off melt inclu-
1197 sions recording shallower entrapment depths, before the crystal cargo was drained
1198 back down in the SC reservoir, and out along the ERZ conduit. It is also possible
1199 that the two reservoir systems always have a higher degree of connectivity than in-
1200 dicated by schematic diagrams such as Fig. 11, with frequent cycling of melt and
1201 crystals between the two reservoirs (and it is simply chance that these lower pressure
1202 inclusions were not seen in the May-18 sample). Further investigation of geophysical
1203 datasets from the 2018 eruption should provide tighter constraints on the depth of
1204 rift zone transport and dike propagation, allowing more rigorous assessments of the
1205 magma transport geometries indicated by our barometric estimates. Additionally,
1206 more detailed work on timescales from diffusive re-equilibration of Fe-Mg in both
1207 melt inclusions and host crystals will help evaluate differences between the High-Fo
1208 crystal cargo erupted at F8 between May and August.

1209 **6 Conclusion**

1210 Detailed investigations of melt inclusion volatile systematics from the 2018
1211 eruption of Kīlauea reveal that the erupted crystal cargo originated from both the
1212 Halema'uma'u reservoir (Low-Fo olivines; $\sim 1\text{--}2$ km depth) and the South Caldera
1213 reservoir (High-Fo olivines, $\sim 3\text{--}5$ km depth). Our work demonstrates that in ad-
1214 dition to the supply of magma from the HMM reservoir inferred from geophysical
1215 modelling of the summit collapse (Anderson et al., 2019), a substantial volume of
1216 magma must also have been derived from the SC reservoir in order to transport
1217 these High-Fo crystals to the surface. This interpretation is consistent with recent
1218 estimates of the total amount of SO_2 emitted from F8 (Kern et al., 2020), which
1219 requires the erupted volume to have been approximately twice that inferred to have
1220 drained from the HMM reservoir by Anderson et al. (2019).

1221 High-Fo Melt inclusions, which mostly yield entrapment depths that are
1222 aligned with geophysical estimates of the depth of the SC reservoir ($\sim 3\text{--}5$ km), host
1223 the vast majority of their CO_2 budget in the vapor bubble ($\sim 90\%$). This is a conse-
1224 quence of the large amounts of PEC experienced by these melt inclusions following
1225 their entrainment into cooler, lower Mg# melts. Based on the textural and chemical
1226 similarities of these High-Fo crystals and those observed at previous eruptions at
1227 Kīlauea (Wieser, Edmonds, et al., 2020; Wieser et al., 2019), we suggest that these

1228 olivines grew from high MgO melts present at the base of the SC reservoir (Helz
1229 et al., 2015), and settled into mush piles for prolonged time periods. Based on the
1230 degree of Mg# re-equilibration between melt inclusions and host olivines, we sug-
1231 gest that these olivines were mobilized from mush piles and mixed into lower Mg#
1232 carrier melts approximately a month to a year before they erupted at Fissure 8.
1233 This disturbance may correspond with the onset of geophysical signals of inflation
1234 in March-April, 2018, interpreted to represent the injection of new melts into the
1235 plumbing system, or a reduction in output from the summit reservoir (Flinders et
1236 al., 2020; Patrick et al., 2020). Because of the large amount of CO₂ in the vapour
1237 bubbles of these inclusions, entrapment depths calculated using only glass CO₂ con-
1238 tents would yield anomalously low entrapment depths (~0.3–0.5 km), and fail to
1239 recognise that the SC reservoir supplied significant volumes of magma to Fissure 8.

1240 In contrast, Low-Fo melt inclusions are closer to equilibrium with their car-
1241 rier melts, so have experienced smaller amounts of PEC. Where present, the vapor
1242 bubble in these melt inclusions is very CO₂-poor, and grew most of its volume dur-
1243 ing during syn-eruptive quenching (~90%). As the quench rates of these samples
1244 mean that there was almost no diffusion of CO₂ between the melt and bubble during
1245 this growth phase, reconstructions of bubble CO₂ contents using equation of state
1246 methods yield anomalously high entrapment depths (4.5–16.1 km; Fig. 11c).

1247 Careful choice of a CO₂-H₂O solubility model is also vital to obtain accurate
1248 entrapment pressures, and therefore depths. Importantly, the basaltic functions of
1249 VolatileCalc, which has been used by the majority of previous Kīlauean melt in-
1250 clusion studies, overpredict entrapment pressures for High-Fo melt inclusions, due
1251 to the simplified relationship between CO₂ solubility and melt composition in this
1252 model. Like EOS methods, use of this model would indicate that ~50% of melt in-
1253 clusions crystallized deeper than the base of the SC reservoir at >5 km (requiring
1254 the presence of a previously unrecognised storage reservoir; Fig. 10).

1255 Overall, our study highlights the importance of measuring bubble densities us-
1256 ing Raman Spectroscopy in addition to measurements of the melt phase by SIMS or
1257 FTIR. We also emphasize the importance of carefully evaluating the compositional
1258 range of different solubility models relative to the melt composition of interest. The
1259 strong agreement between our entrapment depths and models of magma storage

1260 inferred from geophysical datasets at Kīlauea shows that melt inclusion records are
1261 a powerful tool to accurately constrain the location of magma storage reservoirs
1262 supplying volcanic eruptions.

1263 **Acknowledgments**

1264 This work was funded through a NERC DTP studentship to PW (NE/L002507/1),
1265 a NERC ion microprobe grant (IMF675/1118), two Cambridge University Leave to
1266 Work away grants, and a grant from the NERC Centre for Observation and Mod-
1267 elling of Earthquakes, Volcanoes and Tectonics (COMET). We thank Iris Buisman
1268 for help collecting EPMA data, Cees-Jan de Hoog and John Craven at the Edin-
1269 burgh Ion Microprobe Facility for their assistance collecting SIMS data, and Richard
1270 Taylor (Zeiss) for collecting the EDS maps shown in the Supporting Information.
1271 We thank Emily Mason, Emma Liu, and Dave Schneider for help collecting samples
1272 in the field. We are very grateful to Jonathon Tucker to helping us to reproduce the
1273 EOS calculations in his paper, and for helpful discussions about bubble walls. Fi-
1274 nally, we thank Paul Wallace, Kendra Lynn and one anonymous reviewer, along with
1275 the editor Ken Rubin for their helpful comments that greatly improved the quality
1276 of this manuscript.

1277 **Data Availability** The melt inclusion and glass compositions presented in
1278 this paper are provided as an excel spreadsheet. This data has been uploaded to
1279 the Cambridge University Repository <https://doi.org/10.17863/CAM.60202>, and
1280 is also available on Github <https://github.com/PennyWieser/G3-2018-MI>. This
1281 spreadsheet also contains the results of the bubble growth models shown in Fig. 9.

1282 **References**

- 1283 Anderson. (1974). Evidence for a picritic, volatile-rich magma beneath Mt. Shasta,
1284 California. *Journal of Petrology*, 15(2), 243–267.
- 1285 Anderson, & Brown, G. G. (1993). CO₂ contents and formation pressures of some
1286 Kilauean melt inclusions. *American Mineralogist*, 78(7-8), 794–803.
- 1287 Anderson, Johanson, I. A., Patrick, M., Gu, M., Segall, P., Poland, M. P., . . . Mik-
1288 lius, A. (2019). Magma reservoir failure and the onset of caldera collapse at
1289 kīlauea volcano in 2018. *Science*, 366(6470).
- 1290 Antoshechkina, P. M., & Ghiorso, M. S. (2018). MELTS for MATLAB: A new edu-

- 1291 cational and research tool for computational thermodynamics. *AGUFM, 2018*,
1292 ED44B-23.
- 1293 Aster, E. M., Wallace, P. J., Moore, L. R., Watkins, J., Gazel, E., & Bodnar, R. J.
1294 (2016). Reconstructing CO₂ concentrations in basaltic melt inclusions using
1295 raman analysis of vapor bubbles. *Journal of Volcanology and Geothermal*
1296 *Research, 323*, 148–162.
- 1297 Baker, S., & Amelung, F. (2012). Top-down inflation and deflation at the summit of
1298 Kīlauea volcano, Hawaii ‘i observed with InSAR. *Journal of Geophysical Research:*
1299 *Solid Earth, 117*(B12).
- 1300 Barth, A., Newcombe, M., Plank, T., Gonnermann, H., Hajimirza, S., Soto, G. J.,
1301 ... Hauri, E. (2019). Magma decompression rate correlates with explosivity
1302 at basaltic volcanoes—constraints from water diffusion in olivine. *Journal of*
1303 *Volcanology and Geothermal Research, 387*, 106664.
- 1304 Bell, I. H., Wronski, J., Quoilin, S., & Lemort, V. (2014). Pure and pseudo-pure
1305 fluid thermophysical property evaluation and the open-source thermophysical
1306 property library CoolProp. *Industrial & Engineering Chemistry Research, 53*(6),
1307 2498–2508.
- 1308 Bennett, E. N., Jenner, F. E., Millet, M.-A., Cashman, K. V., & Lissenberg, C. J.
1309 (2019). Deep roots for mid-ocean-ridge volcanoes revealed by plagioclase-
1310 hosted melt inclusions. *Nature, 572*(7768), 235–239.
- 1311 Cervelli, P. F., & Miklius, A. (2003). The shallow magmatic system of Kīlauea vol-
1312 cano. *US Geological Survey Professional Paper, 1676*, 149–163.
- 1313 Chakraborty, S. (2010). Diffusion coefficients in olivine, wadsleyite and ringwoodite.
1314 *Reviews in Mineralogy and Geochemistry, 72*(1), 603–639.
- 1315 Clague, D., & Denlinger, R. (1994). Role of olivine cumulates in destabilizing the
1316 flanks of Hawaiian volcanoes. *Bulletin of Volcanology, 56*(6-7), 425–434.
- 1317 Clague, D., Moore, J., Dixon, J., & Friesen, W. (1995). Petrology of submarine lavas
1318 from Kīlauea’s Puna ridge, Hawaii. *Journal of Petrology, 36*(2), 299–349.
- 1319 Collins, S., MacLennan, J., Pyle, D., Barnes, S.-J., & Upton, B. (2012). Two phases
1320 of sulphide saturation in Réunion magmas: Evidence from cumulates. *Earth*
1321 *and Planetary Science Letters, 337*, 104–113.
- 1322 Danyushevsky, L., Della-Pasqua, F., & Sokolov, S. (2000). Re-equilibration of melt
1323 inclusions trapped by magnesian olivine phenocrysts from subduction-related

- 1324 magmas: petrological implications. *Contributions to Mineralogy and Petrology*,
1325 138(1), 68–83.
- 1326 Danyushevsky, L., & Plechov, P. (2011). Petrolog3: Integrated software for modeling
1327 crystallization processes. *Geochemistry, Geophysics, Geosystems*, 12(7).
- 1328 Danyushevsky, L., Sokolov, S., & Falloon, T. J. (2002). Melt inclusions in olivine
1329 phenocrysts: using diffusive re-equilibration to determine the cooling history
1330 of a crystal, with implications for the origin of olivine-phyric volcanic rocks.
1331 *Journal of Petrology*, 43(9), 1651–1671.
- 1332 Dixon, J. E. (1997). Degassing of alkalic basalts. *American Mineralogist*, 82(3-4),
1333 368–378.
- 1334 Dixon, J. E., Clague, D. A., & Stolper, E. M. (1991). Degassing history of water,
1335 sulfur, and carbon in submarine lavas from kilauea volcano, hawaii. *The Jour-*
1336 *nal of Geology*, 99(3), 371–394.
- 1337 Dixon, J. E., Clague, D. A., Wallace, P., & Poreda, R. (1997). Volatiles in alkalic
1338 basalts from the north arch volcanic field, hawaii: extensive degassing of deep
1339 submarine-erupted alkalic series lavas. *Journal of Petrology*, 38(7), 911–939.
- 1340 Dixon, J. E., Stolper, E. M., & Holloway, J. R. (1995). An experimental study of
1341 water and carbon dioxide solubilities in mid-ocean ridge basaltic liquids. part i:
1342 calibration and solubility models. *Journal of Petrology*, 36(6), 1607–1631.
- 1343 Duan, Z., & Zhang, Z. (2006). Equation of state of the h₂o, co₂, and h₂o–co₂ sys-
1344 tems up to 10 gpa and 2573.15 k: Molecular dynamics simulations with ab
1345 initio potential surface. *Geochimica et cosmochimica acta*, 70(9), 2311–2324.
- 1346 Eaton, J. P., & Murata, K. (1960). How volcanoes grow. *Science*, 132(3432), 925–
1347 938.
- 1348 Esposito, R., Bodnar, R., Danyushevsky, L., De Vivo, B., Fedele, L., Hunter, J.,
1349 ... Shimizu, N. (2011). Volatile evolution of magma associated with the
1350 solchiaro eruption in the phlegrean volcanic district (italy). *Journal of Petrol-*
1351 *ogy*, 52(12), 2431–2460.
- 1352 Esposito, R., Klebesz, R., Bartoli, O., Klyukin, Y., Moncada, D., Doherty, A., &
1353 Bodnar, R. (2012). Application of the linkam ts1400xy heating stage to melt
1354 inclusion studies. *Open Geosciences*, 4(2), 208–218.
- 1355 Fermi, E. (1931). Über den ramaneffekt des kohlendioxyds. *Zeitschrift für Physik*,
1356 71, 250-259.

- 1357 Fiske, R. S., & Kinoshita, W. T. (1969). Inflation of kilauea volcano prior to its
1358 1967-1968 eruption. *Science*, *165*(3891), 341–349.
- 1359 Flinders, A., Caudron, C., Johanson, I., Taira, T., Shiro, B., & Haney, M. (2020).
1360 Seismic velocity variations associated with the 2018 lower east rift zone erup-
1361 tion of kilauea, hawaii. *Bulletin of Volcanology*, *82*, 47.
- 1362 Gaetani, G. A., O’Leary, J. A., Shimizu, N., Bucholz, C. E., & Newville, M. (2012).
1363 Rapid reequilibration of h₂O and oxygen fugacity in olivine-hosted melt inclu-
1364 sions. *Geology*, *40*(10), 915–918.
- 1365 Gansecki, C., Lee, R. L., Shea, T., Lundblad, S. P., Hon, K., & Parcheta, C. (2019).
1366 The tangled tale of kilauea’s 2018 eruption as told by geochemical monitoring.
1367 *Science*, *366*(6470).
- 1368 Gerlach, T., McGee, K., Elias, T., Sutton, A., & Doukas, M. (2002). Carbon diox-
1369 ide emission rate of kilauea volcano: Implications for primary magma and the
1370 summit reservoir. *Journal of Geophysical Research: Solid Earth*, *107*(B9),
1371 ECV–3.
- 1372 Ghiorso, M. S., & Gualda, G. A. (2015). An h₂O–CO₂ mixed fluid saturation model
1373 compatible with rhyolite-melts. *Contributions to Mineralogy and Petrology*,
1374 *169*(6), 1–30.
- 1375 Giordano, D., Nichols, A. R., & Dingwell, D. B. (2005). Glass transition tem-
1376 peratures of natural hydrous melts: a relationship with shear viscosity and
1377 implications for the welding process. *Journal of Volcanology and Geothermal*
1378 *Research*, *142*(1-2), 105–118.
- 1379 Gualda, G. A., Ghiorso, M. S., Lemons, R. V., & Carley, T. L. (2012). Rhyolite-
1380 melts: a modified calibration of melts optimized for silica-rich, fluid-bearing
1381 magmatic systems. *Journal of Petrology*, *53*(5), 875–890.
- 1382 Hartley, M. E., MacLennan, J., Edmonds, M., & Thordarson, T. (2014). Reconstruct-
1383 ing the deep CO₂ degassing behaviour of large basaltic fissure eruptions. *Earth*
1384 *and Planetary Science Letters*, *393*, 120–131.
- 1385 Hartley, M. E., Neave, D. A., MacLennan, J., Edmonds, M., & Thordarson, T.
1386 (2015). Diffusive over-hydration of olivine-hosted melt inclusions. *Earth*
1387 *and Planetary Science Letters*, *425*, 168–178.
- 1388 Hauri, E. (2002). Sims analysis of volatiles in silicate glasses, 2: isotopes and abun-
1389 dances in hawaiian melt inclusions. *Chemical Geology*, *183*(1-4), 115–141.

- 1390 Helo, C., Longpré, M.-A., Shimizu, N., Clague, D. A., & Stix, J. (2011). Explosive
 1391 eruptions at mid-ocean ridges driven by co₂-rich magmas. *Nature Geoscience*,
 1392 *4*(4), 260–263.
- 1393 Helz, R., Clague, D., Mastin, L. G., & Rose, T. R. (2015). Evidence for large com-
 1394 positional ranges in coeval melts erupted from kilauea’s summit reservoir.
 1395 *Hawaiian Volcanoes: from Source to Surface*, 125–145.
- 1396 Helz, R., Clague, D. A., Sisson, T. W., & Thornber, C. R. (2014). Petrologic insights
 1397 into basaltic volcanism at historically active hawaiian volcanoes. *US Geological*
 1398 *Survey Professional Paper, 1801*, 237–292.
- 1399 Helz, R., Cottrell, E., Brounce, M. N., & Kelley, K. A. (2017). Olivine-melt relation-
 1400 ships and syneruptive redox variations in the 1959 eruption of kilauea volcano
 1401 as revealed by xanes. *Journal of Volcanology and Geothermal Research, 333*,
 1402 1–14.
- 1403 Helz, R., & Thornber, C. R. (1987). Geothermometry of kilauea iki lava lake, hawaii.
 1404 *Bulletin of Volcanology, 49*(5), 651–668.
- 1405 Iacono-Marziano, G., Morizet, Y., Le Trong, E., & Gaillard, F. (2012). New experi-
 1406 mental data and semi-empirical parameterization of h₂o–co₂ solubility in mafic
 1407 melts. *Geochimica et Cosmochimica Acta, 97*, 1–23.
- 1408 Iacovino, K., Matthews, S., Wieser, P. E., Moore, G. M., & Begue, F. (2020). *Vesi-*
 1409 *cal part i: An open-source thermodynamic model engine for mixed volatile*
 1410 *(h₂o-co₂) solubility in silicate melts.* EarthArxiv. doi: [https://doi.org/](https://doi.org/10.31223/X5D606)
 1411 [10.31223/X5D606](https://doi.org/10.31223/X5D606)
- 1412 Iacovino, K., & Till, C. B. (2019). Densityx: A program for calculating the densities
 1413 of magmatic liquids up to 1,627 c and 30 kbar. *Volcanica, 2*(1), 1–10.
- 1414 Jarosewich, E. (2002). Smithsonian microbeam standards. *Journal of Research of the*
 1415 *National Institute of Standards and Technology, 107*(6), 681.
- 1416 Kauahikaua, J. P., & Trusdell, F. A. (2020). *Have humans influenced volcanic activ-*
 1417 *ity on the lower east rift zone of kilauea volcano? a publication review* (Tech.
 1418 Rep.). HVO: US Geological Survey.
- 1419 Kawakami, Y., Yamamoto, J., & Kagi, H. (2003). Micro-raman densimeter for
 1420 co₂ inclusions in mantle-derived minerals. *Applied spectroscopy, 57*(11), 1333–
 1421 1339.
- 1422 Kern, C., Lerner, A., Elias, T., Nadeau, P. A., Holland, L., Kelly, P. J., ... Cappos,

- 1423 M. (2020). Quantifying gas emissions associated with the 2018 rift erup-
 1424 tion of kīlauea volcano using ground-based doas measurements. *Bulletin of*
 1425 *Volcanology*, 82(7), 1–24.
- 1426 Lamadrid, H., Moore, L., Moncada, D., Rimstidt, J., Burruss, R., & Bodnar, R.
 1427 (2017). Reassessment of the raman co₂ densimeter. *Chemical Geology*, 450,
 1428 210–222.
- 1429 Lee, R. L., Wagoner, L., Conrey, R., Gansecki, C., & Lundblad, S. (2019). *Whole-*
 1430 *rock chemical analyses of lava samples collected during the 2018 lower east*
 1431 *rift zone eruption of kilauea*. U.S. Geological Survey. Retrieved from
 1432 <https://www.sciencebase.gov/catalog/item/5d3279d2e4b01d82ce8791b2>
 1433 doi: 10.5066/P9LVY7GV
- 1434 Lerner, A. (2020). The depths and locations of magma reservoirs and their conse-
 1435 quences for the behavior of sulfur and volcanic degassing. *PhD Thesis, Univer-*
 1436 *sity of Oregon*.
- 1437 Lerner, A., Wallace, P. J., Shea, T., Mourey, A., Kelly, P. J., Nadeau, P. A., ...
 1438 others (2020). Magma source depths and magma recycling in the 2018 erup-
 1439 tion of kīlauea, hawai'i based on volatiles in melt inclusions. In *Agu fall meet-*
 1440 *ing 2020*.
- 1441 Le Voyer, M., Asimow, P. D., Mosenfelder, J. L., Guan, Y., Wallace, P. J., Schiano,
 1442 P., ... Eiler, J. M. (2014). Zonation of h₂o and f concentrations around melt
 1443 inclusions in olivines. *Journal of Petrology*, 55(4), 685–707.
- 1444 Lynn, K. J., Garcia, M., Shea, T., Costa, F., & Swanson, D. A. (2017). Timescales
 1445 of mixing and storage for keanakāko 'i tephra magmas (1500–1820 ce), kīlauea
 1446 volcano, hawai 'i. *Contributions to Mineralogy and Petrology*, 172(9), 76.
- 1447 Maaløe, S., Pedersen, R. B., & James, D. (1988). Delayed fractionation of basaltic
 1448 lavas. *Contributions to Mineralogy and Petrology*, 98(4), 401–407.
- 1449 MacLennan, J. (2017). Bubble formation and decrepitation control the co₂ content of
 1450 olivine-hosted melt inclusions. *Geochemistry, Geophysics, Geosystems*, 18(2),
 1451 597–616.
- 1452 Matzen, A. K., Baker, M. B., Beckett, J. R., & Stolper, E. M. (2011). Fe–mg parti-
 1453 tioning between olivine and high-magnesian melts and the nature of hawaiian
 1454 parental liquids. *Journal of Petrology*, 52(7-8), 1243–1263.
- 1455 Montgomery-Brown, E. K., Sinnett, D., Larson, K., Poland, M. P., Segall, P., &

- 1456 Miklius, A. (2011). Spatiotemporal evolution of dike opening and décollement
 1457 slip at kīlauea volcano, hawai'i. *Journal of Geophysical Research: Solid Earth*,
 1458 *116*(B3).
- 1459 Moore, L. R., Gazel, E., Tuohy, R., Lloyd, A. S., Esposito, R., Steele-MacInnis, M.,
 1460 ... Bodnar, R. J. (2015). Bubbles matter: An assessment of the contribution
 1461 of vapor bubbles to melt inclusion volatile budgets. *American Mineralogist*,
 1462 *100*(4), 806–823.
- 1463 Moore, L. R., Mironov, N., Portnyagin, M., Gazel, E., & Bodnar, R. J. (2018).
 1464 Volatile contents of primitive bubble-bearing melt inclusions from klyuchevskoy
 1465 volcano, kamchatka: Comparison of volatile contents determined by mass-
 1466 balance versus experimental homogenization. *Journal of Volcanology and*
 1467 *Geothermal Research*, *358*, 124–131.
- 1468 Mourey, A., Shea, T., Costa, F., Shiro, B., Oalman, J., Lee, L., & Gansecki,
 1469 C. (2020, August). Preservation of mantle-derived recharge signatures
 1470 in olivine during protracted magma storage. *Goldschmidt Abstracts*,
 1471 *1858*, 1. Retrieved from [https://goldschmidt.info/2020/abstracts/](https://goldschmidt.info/2020/abstracts/abstractView?id=2020003748)
 1472 [abstractView?id=2020003748](https://goldschmidt.info/2020/abstracts/abstractView?id=2020003748) doi: [https://goldschmidt.info/2020/abstracts/](https://goldschmidt.info/2020/abstracts/abstractView?id=2020003748)
 1473 [abstractView?id=2020003748](https://goldschmidt.info/2020/abstracts/abstractView?id=2020003748)
- 1474 Moussallam, Y., Edmonds, M., Scaillet, B., Peters, N., Gennaro, E., Sides, I., &
 1475 Oppenheimer, C. (2016). The impact of degassing on the oxidation state of
 1476 basaltic magmas: a case study of kīlauea volcano. *Earth and Planetary Science*
 1477 *Letters*, *450*, 317–325.
- 1478 Moussallam, Y., Oppenheimer, C., Scaillet, B., Gaillard, F., Kyle, P., Peters, N., ...
 1479 Donovan, A. (2014). Tracking the changing oxidation state of erebus magmas,
 1480 from mantle to surface, driven by magma ascent and degassing. *Earth and*
 1481 *Planetary Science Letters*, *393*, 200–209.
- 1482 Neal, C., Brantley, S., Antolik, L., Babb, J., Burgess, M., Calles, K., ... others
 1483 (2019). The 2018 rift eruption and summit collapse of kīlauea volcano. *Sci-*
 1484 *ence*, *363*(6425), 367–374.
- 1485 Neave, D. A., Hartley, M. E., MacLennan, J., Edmonds, M., & Thordarson, T.
 1486 (2017). Volatile and light lithophile elements in high-anorthite plagioclase-
 1487 hosted melt inclusions from iceland. *Geochimica et Cosmochimica Acta*, *205*,
 1488 100–118.

- 1489 Neave, D. A., Maclennan, J., Edmonds, M., & Thordarson, T. (2014). Melt mixing
1490 causes negative correlation of trace element enrichment and co₂ content prior
1491 to an icelandic eruption. *Earth and Planetary Science Letters*, *400*, 272–283.
- 1492 Newman, S., & Lowenstern, J. B. (2002). Volatilecalc: a silicate melt–h₂O–co₂ solu-
1493 tion model written in visual basic for excel. *Computers & Geosciences*, *28*(5),
1494 597–604.
- 1495 Owen, S., Segall, P., Lisowski, M., Miklius, A., Murray, M., Bevis, M., & Foster, J.
1496 (2000). January 30, 1997 eruptive event on kilauea volcano, hawaii, as moni-
1497 tored by continuous gps. *Geophysical Research Letters*, *27*(17), 2757–2760.
- 1498 Pamukcu, A. S., Gualda, G. A., & Rivers, M. L. (2013). Quantitative 3d pet-
1499 rography using x-ray tomography 4: Assessing glass inclusion textures with
1500 propagation phase-contrast tomography. *Geosphere*, *9*(6), 1704–1713.
- 1501 Patrick, M., Dietterich, H., Lyons, J., Diefenbach, A., Parcheta, C., Anderson, . . .
1502 Kauhikaua, J. (2019). Cyclic lava effusion during the 2018 eruption of kilauea
1503 volcano. *Science*, *366*(6470).
- 1504 Patrick, M., Houghton, B., Anderson, K., Poland, M., Montgomery-Brown, E., Jo-
1505 hanson, I., . . . Elias, T. (2020). The cascading origin of the 2018 kilauea
1506 eruption and implications for future forecasting. *Nature Communications*.
- 1507 Pietruszka, A. J., Marske, J. P., Heaton, D. E., Garcia, M. O., & Rhodes, J. M.
1508 (2018). An isotopic perspective into the magmatic evolution and architecture
1509 of the rift zones of kilauea volcano. *Journal of Petrology*, *59*(12), 2311–2352.
- 1510 Poland, M. P., Miklius, A., & Montgomery-Brown, E. K. (2015). Magma supply,
1511 storage, and transport at shield-stage hawaiian volcanoes. *US Geological Sur-
1512 vey Professional Paper*, *1801*, 179–234.
- 1513 Rasmussen, D. J., Plank, T. A., Wallace, P. J., Newcombe, M. E., & Lowenstern,
1514 J. B. (2020). Vapor-bubble growth in olivine-hosted melt inclusions. *American
1515 Mineralogist: Journal of Earth and Planetary Materials*, *105*(12), 1898–1919.
- 1516 Riker, J. (2005). *The 1859 eruption of mauna loa volcano, hawai'i: Controls on the
1517 development of long lava channels* (Unpublished doctoral dissertation). Univer-
1518 sity of Oregon.
- 1519 Roedder, E. (1979). Origin and significance of magmatic inclusions. *Bulletin de Min-
1520 eralogie*, *102*(5), 487–510.
- 1521 Roedder, E. (1984). Fluid inclusions. *Reviews in mineralogy: Mineralogical Society*

- 1522 *of American, v. 12.*
- 1523 Roeder, P., & Emslie, R. (1970). Olivine-liquid equilibrium. *Contributions to Miner-*
1524 *alogy and Petrology, 29(4), 275–289.*
- 1525 Rosso, K., & Bodnar, R. (1995). Microthermometric and raman spectroscopic
1526 detection limits of CO₂ in fluid inclusions and the raman spectroscopic charac-
1527 terization of CO₂. *Geochimica et Cosmochimica Acta, 59(19), 3961–3975.*
- 1528 Ruth, D. C., Costa, F., de Maisonrouve, C. B., Franco, L., Cortés, J. A., & Calder,
1529 E. S. (2018). Crystal and melt inclusion timescales reveal the evolution of
1530 magma migration before eruption. *Nature Communications, 9(1), 2657.*
- 1531 Ryan, M. P., & Sammis, C. G. (1981). The glass transition in basalt. *Journal of*
1532 *Geophysical Research: Solid Earth, 86(B10), 9519–9535.*
- 1533 Schneider, C. A., Rasband, W. S., & Eliceiri, K. W. (2012). Nih image to imagej: 25
1534 years of image analysis. *Nature methods, 9(7), 671–675.*
- 1535 Shea, T., Hammer, J. E., Hellebrand, E., Mourey, A. J., Costa, F., First, E. C., . . .
1536 Melnik, O. (2019). Phosphorus and aluminum zoning in olivine: contrast-
1537 ing behavior of two nominally incompatible trace elements. *Contributions to*
1538 *Mineralogy and Petrology, 174(10), 85.*
- 1539 Shishkina, T., Botcharnikov, R., Holtz, F., Almeev, R., & Portnyagin, M. V. (2010).
1540 Solubility of H₂O- and CO₂-bearing fluids in tholeiitic basalts at pressures up to
1541 500 mpa. *Chemical geology, 277(1-2), 115–125.*
- 1542 Shishkina, T., Botcharnikov, R. E., Holtz, F., Almeev, R. R., Jazwa, A. M., & Jaku-
1543 biak, A. A. (2014). Compositional and pressure effects on the solubility of H₂O
1544 and CO₂ in mafic melts. *Chemical Geology, 388, 112–129.*
- 1545 Sides, I., Edmonds, M., MacLennan, J., Houghton, B. F., Swanson, D., & Steele-
1546 MacInnis, M. J. (2014). Magma mixing and high fountaining during the
1547 1959 Kīlauea Iki eruption, Hawaii. *Earth and Planetary Science Letters, 400,*
1548 *102–112.*
- 1549 Sides, I., Edmonds, M., MacLennan, J., Swanson, D., & Houghton, B. (2014). Erup-
1550 tion style at Kīlauea volcano in Hawaii linked to primary melt composition.
1551 *Nature Geoscience, 7(6), 464–469.*
- 1552 Skirius, C. M., Peterson, J. W., & Anderson. (1990). Homogenizing rhyolitic glass
1553 inclusions from the Bishop tuff. *American Mineralogist, 75(11-12), 1381–1398.*
- 1554 Span, R., & Wagner, W. (1996). A new equation of state for carbon dioxide covering

- 1555 the fluid region from the triple-point temperature to 1100 k at pressures up to
1556 800 mpa. *Journal of physical and chemical reference data*, 25(6), 1509–1596.
- 1557 Steele-Macinnis, M., Esposito, R., & Bodnar, R. J. (2011). Thermodynamic model
1558 for the effect of post-entrapment crystallization on the h₂O–CO₂ systematics
1559 of vapor-saturated, silicate melt inclusions. *Journal of Petrology*, 52(12),
1560 2461–2482.
- 1561 Taracsák, Z., Hartley, M., Burgess, R., Edmonds, M., Iddon, F., & Longpré, M.
1562 (2019). High fluxes of deep volatiles from ocean island volcanoes: Insights from
1563 el hierro, canary islands. *Geochimica et Cosmochimica Acta*, 258, 19–36.
- 1564 Teasdale, R., Geist, D., Kurz, M., & Harpp, K. (2005). 1998 eruption at volcán
1565 cerro azul, galápagos islands: I. syn-eruptive petrogenesis. *Bulletin of volcanol-
1566 ogy*, 67(2), 170–185.
- 1567 Thornber, C. R., Orr, T. R., Heliker, C., & Hoblitt, R. P. (2015). Petrologic testa-
1568 ment to changes in shallow magma storage and transport during 30+ years of
1569 recharge and eruption at kilauea volcano, hawaii ‘i. *Hawaiian Volcanoes: From
1570 Source to Surface*, 208, 147.
- 1571 Tucker, J. M., Hauri, E. H., Pietruszka, A. J., Garcia, M. O., Marske, J. P., & Trus-
1572 dell, F. A. (2019). A high carbon content of the hawaiian mantle from olivine-
1573 hosted melt inclusions. *Geochimica et Cosmochimica Acta*, 254, 156–172.
- 1574 Tuohy, R. M., Wallace, P. J., Loewen, M. W., Swanson, D. A., & Kent, A. J. (2016).
1575 Magma transport and olivine crystallization depths in kilauea’s east rift zone
1576 inferred from experimentally rehomogenized melt inclusions. *Geochimica et
1577 Cosmochimica Acta*, 185, 232–250.
- 1578 Venugopal, S., Schiavi, F., Moune, S., Bolfan-Casanova, N., Druitt, T., & Williams-
1579 Jones, G. (2020). Melt inclusion vapour bubbles: the hidden reservoir for
1580 major and volatile elements. *Scientific Reports*, 10(1), 1–14.
- 1581 Vinet, N., & Higgins, M. D. (2010). Magma solidification processes beneath ki-
1582 lauea volcano, hawaii: A quantitative textural and geochemical study of the
1583 1969–1974 mauna ulu lavas. *Journal of Petrology*, 51(6), 1297–1332.
- 1584 Wallace, P. J., & Anderson. (1998). Effects of eruption and lava drainback on the
1585 h₂O contents of basaltic magmas at kilauea volcano. *Bulletin of Volcanology*,
1586 59(5), 327–344.
- 1587 Wallace, P. J., Kamenetsky, V. S., & Cervantes, P. (2015). Special collection:

- 1588 Glasses, melts, and fluids, as tools for understanding volcanic processes and
1589 hazards. melt inclusion CO_2 contents, pressures of olivine crystallization, and
1590 the problem of shrinkage bubbles. *American Mineralogist*, 100(4), 787–794.
- 1591 Wang, W., Caumon, M.-C., Tarantola, A., Pironon, J., Lu, W., & Huang, Y. (2019).
1592 Raman spectroscopic densimeter for pure CO_2 and $\text{CO}_2\text{-H}_2\text{O-NaCl}$ fluid sys-
1593 tems over a wide pt range up to 360 c and 50 mpa. *Chemical Geology*, 528,
1594 119281.
- 1595 Whitty, R. C., Ilyinskaya, E., Mason, E., Wieser, P. E., Liu, E. J., Schmidt, A., ...
1596 others (2020). Spatial and temporal variations in SO_2 and $\text{PM}_{2.5}$ levels around
1597 Kīlauea volcano, Hawai'i during 2007–2018. *Frontiers in Earth Sciences*, 8, 36.
- 1598 Wieser, P. E., Edmonds, M., Maclennan, J., Jenner, F. E., & Kunz, B. E. (2019).
1599 Crystal scavenging from mush piles recorded by melt inclusions. *Nature Com-
1600 munications*, 10(1), 1–11.
- 1601 Wieser, P. E., Edmonds, M., Maclennan, J., & Wheeler, J. (2020). Microstructural
1602 constraints on magmatic mushes under Kīlauea Volcano, Hawaii. *Nature Com-
1603 munications*, 11(1), 1–14.
- 1604 Wieser, P. E., Jenner, F., Edmonds, M., Maclennan, J., & Kunz, B. E. (2020, Au-
1605 gust). Chalcophile elements track the fate of sulfur at Kīlauea Volcano, Hawaii.
1606 *Geochimica et Cosmochimica Acta*, 282, 245–275. Retrieved from [https://doi
1607 .org/10.1016/j.gca.2020.05.018](https://doi.org/10.1016/j.gca.2020.05.018) doi: 10.1016/j.gca.2020.05.018
- 1608 Wright, T. L., & Fiske, R. S. (1971). Origin of the differentiated and hybrid lavas of
1609 Kīlauea Volcano, Hawaii. *Journal of Petrology*, 12(1), 1–65.